iFlpMosaics: A method for the ratiometric induction and high-throughput comparative analysis of mutant and wildtype cells

Irene Garcia-Gonzalez[1], Stefano Gambera[1], Alvaro Regano[1], Susana F. Rocha[1], Lourdes Garcia-Ortega[1], Mariya Lytvyn[1], Maria S. Sanchez-Muñoz[1], Aroa Garcia-Cabero[1], Ivana Zagorac[1], Wen Luo[1], Macarena Fernández-Chacón[1], Verónica Casquero-Garcia[1], Federica Francesca Lunella[1], Rui Benedito[1].*

1-Molecular Genetics of Angiogenesis Group, Centro Nacional de Investigaciones Cardiovasculares (CNIC), Madrid, Spain.

* Corresponding author. Rui.Benedito@cnic.es

In order to understand gene function, cells mutated for a gene need to be analysed and compared with normal cells. In most biomedical studies this comparative analysis is carried out with cells present in independent animals and therefore not experiencing the same microenvironment or epigenetic changes. Here we present a large set of new genetic tools and mouse lines that enable the Flp recombinase-dependent mosaic induction and single cell clonal tracking of multiple fluorescently labelled normal and Cre-mutant cells from distinct or the same progenitor cells. The induced cells can be profiled *in situ* by direct multispectral imaging, or by FACS and scRNA-seq. Since with these new tools normal and mutant cells are ratiometrically induced and multispectrally barcoded in the same temporal window and tissue microenvironment, they enable us to understand with higher accuracy and reliability how induced genetic mutations affect the biology of single cells, during tissue development, homeostasis or in disease.

Introduction

When a gene is deleted or mutated in a cell, it generates a cascade of events that may result in a significant change in a cell´s and surrounding tissue phenotype over time. Often scientists analyse mutant cells or tissues that carry genetic mutations for several days, weeks, months or even years and compare their phenotype with independent control cells or tissues of distinct non-mutant (control) animals. During the process of gene mutation to phenotypic manifestation or analysis, often the targeted and surrounding tissue biology changes significantly, which may interact with and change the final phenotype of the mutant cells. An example of this, is the conditional deletion or activation of genes important for vascular, neuronal or cancer development. Mutations that impact tissue function or development, frequently result in a change of the surrounding tissues. Since the non-targeted tissues that surround mutant cells are themselves the source of many biochemical factors, their abnormal

development or function results in the change of a key feedback mechanism that impacts the phenotype of the mutant cells, in a non-cell-autonomous manner, and independently of the initially induced genetic mutation itself (Hansen and Hippenmeyer, 2020; Hansen et al., 2022). This often generates secondary mutant tissue phenotypes over time, that may confound the interpretation of the real or primary gene function on a mutant cell phenotype.

Genetic mosaics are a particularly powerful research tool to overcome these problems because they allow the study of genetic cell-autonomous effects when distinct mutant and control (wildtype) cells arise from the same progenitor cells, and confront the same microenvironment, in the same tissue or organism. In this case, the only difference between the cells used for comparative analysis is the induced mutation in an otherwise identical organism, genetic background and tissue microenvironment.

Mouse models that allow the timed-induction of somatic genetic mosaics are therefore essential to perform the accurate comparative analysis of how control and mutant cell phenotypes develop over time in the same microenvironment. They also represent the only way to accurately study and model biological processes involving sporadic somatic mutations and their effect on cell proliferation, differentiation or competition.

In Drosophila, interchromosomal mitotic recombination associated with distinct tissue markers has been widely used to induce and track genetic mosaics. A similar approach, named as MADM (mosaic analysis with double markers), has been developed in mice allowing the labeling of control and mutant (gene knockout) cells with different fluorescent markers (Contreras et al., 2021; Zong, 2014; Zong et al., 2005). This method has the advantage of allowing the full correlation between the expression of a given fluorescent marker and the genetic status (wildtype, heterozygous or knockout) of the locus carrying the mutation significantly decreasing the rate of false positives or false negatives. However, the method relies on difficult to achieve interchromosomal Cre-dependent recombination events, which overall leads to the generation of very few clones of labelled control and mutant cells in a tissue expressing the recombinase Cre. Due to the rare nature of the interchromosomal recombination events, these genetic mosaics cannot be efficiently induced with tamoxifen-inducible CreERT2 lines, which are weaker and only transiently active. In addition, this technology cannot be used in quiescent cells and requires the chromosomal genetic linkage between the engineered MADM elements and another gene mutation, which significantly complicates the required mouse breedings and genetics and limits its general applicability. MADM is also not compatible with epistasis analysis requiring the simultaneous loss-of-function of multiple genes present in distinct chromosomes, or with the immense variety of existing floxed gain-of-function and loss-of-function alleles.

Given the higher complexity and limitations of MADM, the most widely used method to generate conditional somatic genetic-mosaics in the mouse still involves the much simpler CreERT2-dependent mosaic induction of floxed genes deletion. With this method, the location, timing and frequency of the

recombination events can be regulated by restricting the expression of CreERT2 to a given tissue, and by varying the timing and dosage of the CreERT2 ligand tamoxifen. This much simpler and alternative method needs the use of independent fluorescent reporters of Cre-recombination, in order to detect cells having CreERT2 activity. However, several studies have shown that Cre-activity reporter alleles, only accurately report recombination of themselves, and cannot be used to reliably report recombination of existing floxed alleles (Fernandez-Chacon et al., 2019; Liu et al., 2013; Schmidt-Supprian and Rajewsky, 2007). Though easier to implement than MADM, CreERT2-dependent genetic mosaic approaches generate a high frequency of false positives and false negatives and should not be used to perform mosaic genetics.

To overcome the limitations of current methods to generate genetic mosaics in mice, we have developed *iFlpMosaics*. These consist in a large set of new genetic tools and mouse lines that enable FlpO or Dre-recombinase-dependent-induction of multispectral and ratiometric mosaics of wildtype and mutant cells in the same tissue of an animal. *iFlpMosaics* are compatible with the use of all existent floxed alleles and can be induced in any tissue quiescent or progenitor cells. They also allow a much tighter control over time of the frequency of genetic mosaicism. The multiple fluorescent labels match with high certainty the genetic status of the cells, that can be either control/wildtype or mutant for one or several genes. Since the multispectral and genetic barcoding of the cells is ratiometric, single-cell derived mutant and wildtype clonal expansion and differentiation can be profiled with high accuracy directly *in situ* through imaging or by FACS or scRNAseq. *iFlpMosaics* will greatly facilitate the induction and analysis of somatic genetic mosaics and turn possible the understanding how an individual or combinatorial set of genetic mutations affect the biology of single cells during tissue development, regeneration or disease.

False positives and false negatives with Cre-dependent mosaic genetics

Given its simplicity, CreERT2 genetics is still the most frequently used technique to induce and study single cell or tissue-specific genetic mosaics in mice. However, it is prone to induce a high frequency of false positives and false negatives. False positives are defined as cells recombining/expressing a reporter, and not having another independent floxed reporter or gene deleted. Conversely, false negatives are defined as cells not having a specific reporter allele recombined, but having another floxed reporter or gene deleted (Fig. 1a). The high frequency of false positive and false negative cells has been previously reported (Fernandez-Chacon *et al.*, 2019; Liu *et al.*, 2013) but so far no study has systematically quantified their occurrence for multiple reporter alleles and at different CreERT2 induction rates or tamoxifen doses, that are frequently used in mosaic genetics. In order to do this, we decided to analyse several independent mice containing multiple Rosa26 reporters that could

allow us to detect false positives or negatives among different reporters by FACS or by histological analysis. This analysis showed that different Cre-reporters, even when localized in the same accessible Rosa26 locus, and having similar genetic distances between LoxP sites, recombine at significant different relative frequencies (Fig. 1b). As expected, the chance of finding cells having dual recombination of two reporters (true positives) decreased with the decrease in the dose of induction or tamoxifen (Fig. 1c, 1d). It is important to note that for single cell functional genetic/clonal analysis, usually it is necessary to decrease the dose of tamoxifen in order to obtain sparse labelling of mutant or wildtype cells in the tissue. This means achieving between 0.01-10% recombination rate, so that single cells and their clones can be unequivocally distinguished. We found that even at around 10-60% average recombination rate for two independent reporters, with similar sensitivities to CreERT2/4OHT, the rate of true positives was very low (Fig. 1c, 1d).

This data shows that when using standard CreERT2 mosaic genetics, not a single existing Cre-reporter will accurately report the recombination of any other reporter, and certainly also not any other floxed gene. Therefore, the large majority of CreERT2-based functional genetic studies *in vivo* using mosaic genetics or sparse cell labelling, will not achieve the desired targeted gene deletion in labelled cells, and therefore will not be able to uncover the real effect of the gene on single cell biology, with high accuracy and statistical power.

Design and validation of *iFlp-Mosaic* mice

To overcome the caveats of the CreERT2-dependent and MADM mosaic genetics technologies mentioned above, we developed *iFlpMosaics*. This consist in several mouse lines that allow the FlpO/FlpOERT2-recombinase-dependent induction of ratiometric mosaics of fluorescent mutant (gene KO) and normal (gene wildtype) cells (Fig. 1e, 1f and Sup. Fig. 1a, b). We term these new mouse alleles as *iFlp-Mosaics* (R26-$iFlp^{MTomato\text{-}Cre/MYFP}$ and Tg-$iFlp^{MTomato\text{-}H2B\text{-}GFP\text{-}Cre/MYFP\text{-}H2B\text{-}Cherry\text{-}FlpO}$). They contain the ubiquitously expressed CAG promoter and several distinct and mutually exclusive FRT sites (Cai et al., 2013), that enable multispectral labeling and fate-mapping of different mutant (Tomato+ and Cre+) and wildtype (YFP+ and Cre-) cells in any tissue expressing FlpO or FlpOERT2. The two lines differ either in the genomic location (ROSA26 versus random transgene), or the expression of additional chromatin-bound (H2B-tag) fluorescent proteins for increased cellular resolution and quantitative power (Fig. 1e, 1f and Sup. Fig. 1a, b).

Transfection of *iFlp-Mosaic* ES cells with FlpO expressing plasmids or induction of these mosaics in mice carrying FlpO/FlpOERT2 alleles, induced the expected ratiometric mosaic of cells (Fig. 1e, 1f, and Supplementary Fig. 1c-g). The observed ratios of recombination are in agreement with the shorter genetic distance between the FRTF3 sites, in comparison with FRT5T2 sites (Fig. 1e and Sup. Fig. 1e). In both ES cells and mice, the initially induced cellular ratios did not change significantly

141 after prolonged culture or during tissue development *in vivo* (Fig. 1g and Sup. Fig. 1h), showing that
142 expression of MbTomato-2A-Cre (or MbYFP) is not deleterious to cells. Of note, we found on average
143 10 times less expression of the cassette MbTomato-2A-Cre in *iFlp-Mosaic* mice than with the
144 previously generated *iSuRe-Cre* mice (Fig. 1h), which further reduces the occurrence of any potential
145 Cre-toxicity (Fernandez-Chacon *et al.*, 2019). This difference in expression is likely due to the different
146 DNA elements contained in these alleles or their different genomic location and epigenetic regulation.
147 Given the reported transcriptional stop leakiness and germline recombination of previous
148 inducible Cre-expressing alleles located in the Rosa26 locus (Fernandez-Chacon *et al.*, 2019; Lao et al.,
149 2012), even in the absence of FlpO/CreERT2 activity, we checked if *iFlp-Mosaic* mice were also leaky,
150 given that the *iFlp-Mosaic* alleles contained a Cre and also FlpO expressing cassette, that can be
151 expressed if the upstream transcriptional stop signals are bypassed, as in previous mouse lines.
152 Importantly, none of the *iFlpMosaic* mice had leaky expression of the fluorescent proteins contained in
153 their constructs, in the absence of an extra allele expressing FlpO (Sup. Fig. 1i). The combination of
154 *iFlp-Mosaic* mice with *Rosa26*$^{-LSL-YFP}$ reporter mice, revealed a very low % of non-self Cre-leakiness in
155 some organs of the *Tg-iFlp*$^{Tomato-H2B-GFP-Cre/YFP-H2B-Cherry-FlpO}$ mouse line only. This recombination occurs
156 sporadically throughout embryonic development until adult stages, in the absence of any Flp activity,
157 or any detectable *iFlp-Mosaic* fluorescent protein expression (Sup. Fig. 1i). This residual Cre non-self-
158 leakiness is likely due to residual and sporadic skipping or splicing of the 2 polyA transcription STOP
159 cassette that precede the ORF containing Cre, as shown before (Fernandez-Chacon *et al.*, 2019; Lao *et*
160 *al.*, 2012). Importantly, these very few false negative cells detected with the *Rosa26*$^{-LSL-YFP}$ Cre-reporter
161 will never be detected or analysed with *iFlpMosaics*, since they are non-fluorescent in the absence of
162 other Cre-reporter alleles. Significantly more relevant than false negatives, is the ocurrence of false
163 positives. We found that in i*FlpMosaic* mice, MbTomato-2A-Cre+ cells efficiently recombine other
164 Cre-reporter alleles, but also all floxed genes tested (Fig. 1i. 1j), which ensures high genetic reliability
165 at single cell resolution. As an example, induction of *iFlpMosaics* in the *Rbpj* floxed background, a
166 gene known to be essential for arterial development, results in only 3.5% Tomato-2A-Cre+ cells in
167 arteries and 96% in veins and capillaries, indicating how efficient was the deletion of this gene.
168 Altogether, this data shows that with *iFlpMosaics* the rate of properly labelled and assigned mutant and
169 wildtype cells is very high. This is in stark contrast to standard CreERT2 mosaic genetics (Fig. 1c, 1d),
170 and similar to the MADM system (Contreras *et al.*, 2021; Zong, 2014; Zong *et al.*, 2005). Therefore,
171 *iFlpMosaic* alleles enable for the first time the tightly-controlled induction of reliable and ratiometric
172 mosaics of mutant and wildtype cells in any tissue expressing FlpO or FlpOERT2, and provide both
173 membrane and nuclei fluorescent markers to track mutant and wildtype cells proliferation,
174 differentiation or migration with very high cellular and quantitative resolution (Sup. Figure 2).
175
176

177

178 **Generation of ubiquitous and tissue-specific FlpOERT2 mouse lines**

179

180 Multispectral genetic mosaics are a particularly relevant research tool when is possible to
181 induce them at a specific time point and in a significant number of cells, which is not possible to achieve
182 with the MADM system (Contreras *et al.*, 2021; Zong, 2014; Zong *et al.*, 2005). To have temporal
183 control over Flp activity or induction, different mouse lines were generated in the past that enable the
184 constitutive (Rosa26) or tissue-specific expression of FlpeERT or the mammalian codon optimized
185 FlpOERT (Hunter et al., 2005; Kranz et al., 2010). These studies have shown that FlpOERT2 activity
186 is significantly lower than CreERT2, and very few cells in each organ were shown to recombine (Lao
187 *et al.*, 2012). The published $R26^{CAG\text{-}FlpOERT2}$ line recombined the $R26\text{-}iFlp^{MTomato\text{-}Cre/MYFP}$ allele in only
188 around 0.2% of most embryo cells, and was also weak in postnatal and adult organ cells (Fig. 2a).

189 We therefore thought to develop new constructs containing optimized DNA elements (Cai *et*
190 *al.*, 2013; Pontes-Quero et al., 2017) in order to enhance FlpOERT2 expression (Fig. 2b). We generated
191 and screened in total 5 transgenic ubiquitous-FlpOERT2 mouse lines with variable copy number (Fig.
192 2c). Importantly, when comparing with the existing $R26^{CAG\text{-}FlpOERT2}$ line, the best of these new *Tg(Ins-*
193 *CAG-FlpOERT2)* lines (named here as, $Tg(Ins\text{-}CAG\text{-}FlpOERT2)^{\#F2}$) induced several folder higher
194 recombination of the *iFlpMosaic allele* in embryos and different organs and cell types (Fig. 2d-g and
195 Sup. Fig. 3a-d). With this higher frequency of recombination, we could frequently see mutant
196 (MTomato+) and wildtype (MYFP+) cells close to each other, which enables direct comparative
197 analysis of cells experiencing the same tissue microenvironment (Fig. 2f, 2g). Interestingly,
198 recombination was not equal among different cell types and organs. We also confirmed that despite the
199 ubiquitous and strong expression of FlpOERT2 by this new line, it is not leaky (Sup. Fig. 3e). Unlike
200 the published $R26^{CAG\text{-}FlpOERT2}$ allele, this new transgenic allele can also be combined with two other
201 Rosa26 targeted alleles, which is of high utility as it will be shown further below.

202 Besides generating ubiquitous FlpOERT2 lines of general relevance, we also developed a
203 method to easily target and modify pre-existing and pre-validated CreERT2 expressing transgenic
204 alleles, for tissue-specific expression of FlpOERT2. We designed unique guide RNAs and donor DNAs
205 containing FlpO that allow the efficient conversion of CreERT2 alleles into a FlpOERT2 expressing
206 allele (Fig. 2h). Using this method, we converted an existing PAC Cdh5-CreERT2 mouse line (Wang
207 et al., 2010) containing 4 copies of the CreERT2 sequence, to PAC Cdh5-FlpOERT2 mouse lines
208 containing 3 or 4 copies of the FlpOERT2 sequence (Fig. 2i). From the obtained two founder lines, only
209 the line $Cdh5\text{-}FlpOERT2^{F1}$ did not have any residual Cre sequence or activity. As expected, this line
210 was expressed and induced recombination specifically in endothelial cells (Fig.2j).

211
212
213 **Ratiometric functional genetics with *iFlp-Mosaic* mice**

214

215 In contrast to previous classical Cre-reporters or the *iSuRe-Cre* allele, *iFlpMosaics* are
216 ratiometric by design. This allows the quantification by histology or FACS of the relative frequencies
217 (ratio) of mutant (MbTomato-2A-Cre+) and wildtype (MbYFP+) cell populations induced exactly in
218 the same tissue, and experiencing the same microenvironment throughout the pulse-and-chase period.
219 We envisioned this property could be used to study in a high-throughput and accurate manner the cell-
220 autonomous function of genes in virtually all cell types, and for long time periods, something not
221 possible to be done with classical gene knockouts, because of their early lethality or major
222 abnormalities, or with classical Cre/CreERT2 mosaic genetics, because of the high frequency of false
223 positives/negatives (Fig. 1c, 1d), and the lack of an internal induction control of wildtype cells.

224 To demonstrate the power of *iFlpMosaic* mice to understand the effect of induced mutations in
225 multiple cell lineages we intercrossed them with either the *Tg(ACTFLPe)9205Dym* (Rodriguez et al.,
226 2000) allele (abreviated as *ACTB:FlpE - recombines early embryo progenitor cells)*; the *Apln-FlpO*
227 (Luo et al., 2021) allele (recombines endothelial and derived hematopoietic cells) or the new *Tg(Ins-*
228 *CAG-FlpOERT2)* allele (induces recombination at any stage and in all cell type). These alleles were
229 further combined with floxed alleles for the genes *Myc and Foxos*. These genes are known to be
230 important for the proliferation and differentiation of many different cell types (Claveria et al., 2013;
231 Eijkelenboom and Burgering, 2013).

232 When the allele *R26-iFlp*$^{MTomato\text{-}Cre/MYFP}$ was combined with the *ACTB:FlpE* or *Apln-FlpO*
233 alleles and the *Myc and Foxos* floxed alleles, mosaic mutant animals survived until adult stages, unlike
234 embryos carrying mutations of these genes in all cells or in all endothelial cells (Dharaneeswaran et al.,
235 2014; He et al., 2008). To understand how these genes affected the biology of different organ cell types,
236 we first used FACS analysis to score in a high throughput manner the relative ratios of mutant
237 (MTomato-Cre+) and wildtype cells (MYFP+) in several major organs of postnatal day 7 animals. The
238 assumption was that if a gene is really important for a given cell type/organ biology or lineage, it would
239 either change the proliferation or differentiation rate of the mutant cells, and that would be noticed in
240 the final MTomato+/MYFP+ log ratio detectable by FACS. This analysis revealed that the impact of
241 Myc loss varies in different cell types and organs. It was previously proposed that Myc loss leads to a
242 general competitive disadvantage (Claveria *et al.*, 2013) and lack of proliferation by ECs (Wilhelm et
243 al., 2016), however, when deleted mosaicly, it has a relatively minor effect on the clonal expansion of
244 ECs (Fig. 3a). In contrast, we observed blood to be the most sensitive cell type to the mosaic loss of
245 Myc (Fig. 3b and Sup. fig. 4a, b). Most CD31-CD45- lung and heart cells were not significantly affected

246 by Myc deletion (Fig. 3c), likely due to compensation by the homologous *Mycn* gene (Munoz-Martin
247 et al., 2019).

248 We also confirmed the power of the system to perform mosaic epistasis analysis of mutant cells
249 with deletion of multiple genes, in this case 3 *Foxo* genes (6 floxed alleles). Foxos partially compensate
250 the function of each other in several cell types, and together they are considered to be important negative
251 regulators of cell proliferation and metabolism downstream of AKT signalling, preventing uncontrolled
252 cell growth (Eijkelenboom and Burgering, 2013; Wilhelm *et al.*, 2016). Surprisingly, the results show
253 that mosaic deletion of three *Foxo* genes ($Foxo1/3/4^{KO}$) had relatively minor consequences for cell
254 expansion in the liver and lung, and affected especially heart cells (Fig. 3d). This suggests cell-type and
255 organ-specific functions for *Foxos*. The data also showed that postnatal retina ECs are especially
256 responsive to the loss of *Foxo1/3/4*, as they were much more proliferative, formed dense EC clusters,
257 and outcompeted wildtype cells over time (Fig. 3e-g), similarly to what has been shown before using
258 standard CreERT2 genetics (Wilhelm *et al.*, 2016).

259 Overall, these results show the power of this technology to accurately model and analyse in a
260 high-throughput manner by FACS, or tissue imaging, the impact of somatic mutations in cellular
261 expansion and competition. In this particular case, it revealed that MYC and FOXOS are dispensable
262 for the proliferation of many types of cells in diverse organs.

263

264 ***Combining iFlp-Mosaic with iFlp^{Chromatin}* for higher single-cell clonal resolution**

265

266 Direct live imaging of Cre-mutant and adjacent normal fluorescent cells can be one of the main
267 applications of the *iFlp-Mosaic* technology. However, even though live microscopic imaging is routine in
268 many species and developmental model systems, it is still not possible, or practical, for most mouse tissues and
269 laboratories, due to the deep tissue location of most cells in the mouse, lack of appropriate microscopes, or the
270 relatively slow pace of the biological processes under study. To analyse how single cells proliferate,
271 differentiate and migrate in a mouse tissue advanced pulse-and-chase genetic and imaging/analysis tools are
272 required. Genetic tools such as the *Brainbow*, *Confetti* or the *Dual ifgMosaic* were generated for this purpose
273 (Livet et al., 2007; Pontes-Quero *et al.*, 2017; Snippert et al., 2010). When compared with standard unicolor or
274 single-molecule reporters of Cre activity, multispectral mosaics allow a more precise and quantitative single-
275 cell retrospective and clonal lineage tracing, due to the lower probability of a cell having a given stochastic
276 recombination event. To increase the quantitative single cell resolution of the *iFlp-Mosaic* technology, we
277 combined the *Rosa26-iFlp$^{MbTomato\text{-}Cre/MbYFP}$* allele with the published *Rosa26-iChr2-Mosaic* allele (Pontes-
278 Quero *et al.*, 2017). These enables the stochastic and mutually exclusive expression of both chromatin/nuclei
279 (for cell unit count) and membrane (for cell shape) localized fluorescent proteins in mutant (MbTomato-2A-
280 Cre+) cells, expanding the diversity of barcoding from 1 to 3 different possible mutant cells (Fig. 4a).

281 Despite higher clonal resolution in single MbTomato+/mutant cells, this method does not allow us to
282 quantify in the same microenvironment, and with the same level of resolution, how the MbYFP+/wildtype
283 cells clonally expand. In order to have higher clonal resolution also in wildtype cells, we developed the
284 *iFlp*^{Chromatin}*-Mosaic* (or *iFlp*$^{H2B\text{-}Cherry/GFP/Cerulean}$) mouse line, in which three distinct and incompatible FRT sites
285 enable the generation of a Flp-recombinase-dependent mosaic of cells expressing three distinct chromatin (Chr)
286 localized fluorescent proteins (Fig. 4b, 4c). When interbred with the *Tg(Ins-CAG-FlpOERT2)* and
287 *iFlp*$^{MbTomato\text{-}Cre/MbYFP}$*-Mosaic* lines, this new *iFlp*^{Chromatin}*-Mosaic* allele allow us to generate up to 8 different
288 dual-labelled cells (4 mutant and 4 wildtype), significantly increasing the single-cell clonal lineage tracing
289 resolution of both mutant and wildtype cells in the same tissue microenvironment (Fig. 4d). The alleles above
290 can also be combined with the published Cre-dependent Tg*iMb2-Mosaic* allele or *iCre*$^{MYFP/Tomato/MTFP1}$
291 (Pontes-Quero *et al.*, 2017), to have even higher single-cell or clonal resolution on mutant (Tomato+/Cre+, 12
292 different) and wildtype (YFP+, 4 different) cells (Fig. 4e). This technology also allows us to identify and
293 label binucleated or polyploid cells, such as adult liver hepatocytes (Fig. 4f).

294 As an example, we show here how these new mouse alleles and technology enabled us to
295 achieve very high cellular resolution, and the accurate quantification how single mutant and wildtype cells
296 clonally expand, or survive, when induced at the same time, in the same tissue microenvironment.

297 In the liver, a high % of neonatal hepatocytes are in S-phase (EdU+) or in cycle (Ki67+) at P1
298 and P7 and most stop dividing before P20 (Fig. 5a), however their single cell clonal expansion dynamics
299 is still unknown. *iFlp-Mosaic x iFlp*^{Chromatin} mice were induced at P1 and livers collected at P20 for
300 multispectral imaging and single-cell clonal analysis. The clone maps revealed that hepatocyte proliferation
301 (clones with 2 cells or more) were dispersed across the liver (Fig. 5b and Sup. Fig. 5a,b). The recombination
302 frequency varied among animals, but the relative distribution and average clone size of wildtype cells was still
303 similar (Fig. 5c), confirming that there is enough multispectral clonal and quantitative resolution at both low
304 and high *iFlp-Mosaic* recombination frequencies. This data revealed that 17,2% of postnatal hepatocytes did
305 not expand clonally, with the majority of hepatocytes (69%) dividing only once or twice in 20 days. Only 2.4%
306 of single hepatocytes gave clones with 8 or more cells. The average clone size of wildtype cells was around 2.9
307 (Fig. 5b, c). These clonal dynamics is in absolute agreement with the observed 2.9-fold liver weight increase
308 from P1 to 20 (Fig. 5d). We than compared the clonal expansion of wildtype (MYFP+) and mutant *Myc*^{KO}
309 (Mtomato-2A-Cre+) hepatocytes. This revealed that MYC is necessary for optimal postnatal hepatocytes
310 clonal expansion. On average, *Myc*^{KO} hepatocytes clone size was 2.25 and these generated only 125% (125
311 new hepatocytes for each 100) more hepatocytes over 20 days, whereas wildtype cells clone size was 2.87 and
312 these generated 187% more hepatocytes, over the same period (Fig. 5e,f).

313 We next performed a similar single cell clonal expansion analysis of postnatal pancreatic cells. These
314 cells had similar Ki67+ and EdU+ frequencies as liver cells (compare Fig.5a with Sup. Fig. 5c, d). However,
315 *iFlpMosaics* analysis revealed that wildtype pancreatic cells expand significantly more than hepatocytes until

316 P20 (average clone size 3.60 instead of 2.87, compare Wt values in Fig. 5g-i with Fig.5e,f). In the pancreas,
317 *Myc*^{KO} cells also expanded significantly less (Fig. 5h, 5i) and at the end were 3.7 fold less frequent than
318 neighbouring wildtype cells (Fig. 5j).

319 Recent work proposed the existence of a highly proliferative hepatocyte population in adult livers,
320 based on a new Dre-inducible Ki67-Cre (ProTracer) allele (He et al., 2021). Ki67 immunostaining showed that
321 only 1.87% of adult liver hepatocytes are in cycle at a given moment (Sup. Fig.5d). Of note, Ki67 may be
322 expressed in metabolically activated (primed and in cycle) or DNA replicating (S-phase), or polyploid cells,
323 but many Ki67+ cells may not undergo productive cell division, or die after being in cycle. Our *iFlpMosaics*
324 can measure both productive cell expansion or cell survival. Using the *iFlpMosaic* mice with the highest
325 number of multispectral combinations, and therefore clonal resolution, we observed very limited proliferation
326 or clonal expansion of single mononucleated or binucleated hepatocytes during the 2 weeks after induction.
327 Average clone size of wildtype adult hepatocytes was only 1.10 (Fig. 5k, l). In 2 weeks, only 9.5% of single
328 mononucleated or binucleated diploid hepatocytes underwent productive division or cytokinesis from
329 binucleated cells to form a 2-cell clone (Fig. 5m, n). Frequency of proliferation was also low among polyploid
330 hepatocytes (4.9%). This data significantly extends on the recent analysis of hepatocytes proliferation
331 dynamics using the ProTracer technology (He *et al.*, 2021).

332 Despite the absence of significant hepatocytes proliferation in homeostasis, when we induced the *iFlp*
333 ratiometric mosaics in adult *Myc*^{flox} livers, we still observed a very significant loss (4.2 fold decrease) of mutant
334 *Myc*^{KO} (Mtomato-2A-Cre+) cells in only 2 weeks after induction (Fig. 5o). Given the absence of significant
335 clonal expansion of wildtype cells in adult livers (Fig. 5l - average clone size 1.10, meaning only 10 more
336 hepatocytes for each 100 hepatocytes in 2 weeks), this data suggests that Myc loss induces a significant
337 decrease in adult hepatocytes survival. Interestingly, wildtype hepatocytes when surrounded by *MycKO*
338 hepatocytes expanded more than when surrounded by wildtype hepatocytes (compare Fig. 5m/n with 5p/q and
339 Sup. Fig.5e), probably to compensate for the loss of *Myc*^{KO} hepatocytes. This data agrees with the existence of
340 a Myc-dependent cell competition among adult hepatocytes, in which cells with lower Myc are less fit and
341 gradually excluded, as shown before to occur during early embryonic development (Claveria *et al.*, 2013).
342 Among the surviving *Myc*^{KO} mutant cells, we also observed a significant increase in the % of binucleated cells,
343 and a decrease in the % of 2-cell mononucleated clones, suggesting that *Myc*^{KO} binucleated hepatocytes
344 undergo cytokinesis less frequently (Sup. Fig. 5e).

345

346 ***iFlp/Dre*^{Progenitor} enables induction of genetic mosaics from single progenitor cells**

347 The results above show also that there is significant intercellular clonal variability, when
348 different progenitor cells, occupying different tissue locations, are induced. This decreases the statistical
349 robustness of the analysis of a gene function in single cells and requires the comparative analysis of a
350 large number of single-cell derived clones, and averaging of clone size differences. With the method

351 above, averaging and population comparisons can be made among all Tomato+ and all YFP+ clones
352 found in a region. However, since they derive from different progenitor cells, is not possible to know
353 exactly how a gene loss, changes the cellular and clonal expansion phenotype of a specific single-cell
354 progeny, located in a particular niche. The existent MADM approach allows the generation of labelled
355 wildtype and mutant cells from the same progenitor cell, and in this way estimate very precisely how a
356 gene mutation impacts on the progeny single cell mobilization and proliferation phenotypes. However,
357 as mentioned above, MADM is very difficult to implement and induce at a specific time point, nor it is
358 compatible with the numerous existent floxed genes.

359 To overcome the limitations of current approaches to understand the role of genes in single
360 progenitor cell biology, we designed the *iFlp/Dre*^{Progenitor} DNA construct. This was injected in mouse
361 eggs to produce transgenic animals, of which only one of four founders was good and named as
362 *iFlp/Dre*$^{Progenitor\ F1}$ (Fig. 6a). We also knocked-in this construct by CRISPR-Cas9 in the *Tg(Ins-CAG-*
363 *FlpOERT2)*$^{\#F4}$ locus creating the dual *Tg(Ins-CAG-FlpOERT2 + iFlp/Dre*^{ProgenitorF2}*)* allele (Fig. 6b).
364 These *iFlp/Dre*^{Progenitor} alleles can be induced by both FlpOERT2, or the stronger DreERT2. Therefore,
365 we also generated a new *Tg(Ins-CAG-DreERT2)*$^{\#F4}$ allele by using CRISPR/Cas9 assisted targeting
366 (Fig. 6c). When these alleles are combined with the *iFlpMosaic* alleles, is possible to induce with
367 tamoxifen a genetic cascade that culminates with the generation of genetic mosaics of mutant and
368 wildtype cells derived from the same single progenitor cell. After tamoxifen induction of FlpOERT2 or
369 DreERT2, the iFlp/Dre-Progenitor allele is recombined, and this triggers the constitutive expression of
370 FlpO, H2B-V5 and the cell-surface marker hCD2. FlpO will than effectively recombine in H2B-
371 V5+/hCD2+ cells the *R26-iFlp*$^{MTomato\text{-}Cre/MYFP}$ allele (Fig. 6d). We hypothesized that since FlpO is a
372 relatively weak recombinase and the transgene takes some time to be fully expressed, it could also take
373 time to recombine the *R26-iFlp*$^{MTomato\text{-}Cre/MYFP}$ allele. During this period, a dividing cell will often
374 generate two or more daughter cells, and in these, the *iFlpMosaic* allele can be recombined in one of
375 two possible ways, generating either Tomato-2A-Cre+ or YFP+ cells within the progeny of a single
376 cell.

377 To test this hypothesis, we induced growing animals with low dose of tamoxifen at P4, and
378 collected tissues for analysis 3 days later at P7. In animals without the *iFlp/Dre*^{Progenitor} allele, Tomato+
379 and YFP+ cells arised from independent progenitors that were genetically pulsed in independent
380 locations and rarely YFP+ wildtype cells were intermixed with mutant Tomato+ cells (Fig. 6e). In
381 animals having the *iFlp/Dre*^{Progenitor} allele, anti-V5 immunostaining enabled the detection of the nuclei
382 of the progenitor cell and its progeny. V5+Tomato+ and V5+YFP+ cells were frequently located close
383 to each other confirming that they arised from a single progenitor cell (Fig. 6f and Sup. Fig. 6a), which
384 allows for direct comparisons of a gene function in the progeny of single progenitor cells.

385 Importantly, the use of the *iFlp/Dre*^{Progenitor} allele also allowed us to significantly increase the
386 sensitivity (14 fold) to FlpOERT2 recombination. Using the Cdh5-FlpOERT2 line we increased EC-
387 recombination efficiency from an average of 3.6% to 51% (Fig. 6g).

388 The use of *Tg(Ins-CAG-DreERT2)*$^{\#F4}$, instead of *Tg(Ins-CAG-FlpOERT2)*$^{\#F4}$, allowed a
389 significant increase in the efficiency of recombination as well (Fig. 6h).
390 Another advantage of the *iFlp/Dre*^{Progenitor} allele is the possibility of using anti-hCD2 magnetic
391 beads or antibodies to quickly isolate the recombined cells, even when their frequency is very low.
392 hCD2+ cells had a 25-fold higher % of Tomato+ and YFP+ cells (Fig. 6i), resulting in a much faster
393 isolation of these cells, which is important when when many tissues or infrequent populations have to
394 be isolated on the same day for scRNAseq analysis.
395
396 **Combining single cell RNA-seq with ratiometric *iFlp*^{Mosaics} to uncover gene function in all cell**
397 **types**

398 Recent advances in single cell RNA sequencing (scRNA-seq) methods have allowed the
399 understanding of single-cell biology in an unprecedented way. There are however three main limitations on the
400 use of scRNAseq technologies to assess the transcriptome of single mutant and wildtype cells resulting from
401 conditional genetic experiments. The first is the introduction of microenvironment changes bias by the profiling
402 of cells obtained from distinct mutant and wildtype animals, that experienced distinct epigenetic and
403 microenvironmental changes during their lifetime or in disease. The second, the reliance on standard Cre-
404 reporters to define and isolate the mutant cells of interest, since, as we showed above (Fig. 1), they do not
405 correlate with desired genetic deletions, particularly in CreERT2 inducible experiments. And the third, and
406 most important, the difficulty in validating a priori that the desired floxed gene has been deleted among the
407 pool of analysed mutant single cells. This is important because scRNAseq technologies only detect the mRNA
408 of some genes in most single cells, and also because many floxed genes conserve their 3´ mRNA
409 sequences after genetic deletion, leading to the transcriptional profile of pseudomutant cells whose true
410 genetic status cannot be accurately determined.

411 We have provided evidence that in contrast to other genetic technologies, the *iFlp-Mosaic*
412 alleles here developed allow the reliable isolation of *bona fide* mutant cells and wildtype cells from the
413 same tissue (Fig. 1 and 2). We also provided evidence how ratiometric *iFlp-Mosaic* cell population
414 genetics based on FACS or histology can be used to easily score the role of genes in single cell biology.
415 Therefore, we decided to test if we could also use scRNA-seq with *iFlpMosaics* to score in a high
416 throughput manner the role of genes (i.e. *Rbpj*) in the proliferation and differentiation of all early
417 embryo cell types. *Rbpj* codes for a transcription factor essential for all Notch signalling, and this is one
418 of the most important pathways for cell proliferation and differentiation during embryonic development
419 (Siebel and Lendahl, 2017). We pulsed embryos with 4-OHT at embryonic day 9.5 (E9.5) and collected
420 Tomato+ (mutant) and YFP+ cells by FACS at E13.5 (Fig. 7a). 16 major cell types were identified
421 based on their transcriptome and previously known marker genes (Fig. 7b). In Tomato-2A-Cre+ cells,
422 *Rbpj* deletion of the exons 6 and 7 generates a more unstable, but still detectable 3´mRNA (Fernandez-
423 Chacon et al., 2023), and a decrease in the expression of *Rbpj* and the main downstream target *Hes1*

424 (Fig. 7c). Deletion of *Rbpj* led to changes in the frequency of cells in S-phase (Ki67+ mRNA) in some
425 clusters (Fig. 7c). *Rbpj* deletion at E9.5, compromised the differentiation or expansion of peripheric
426 nervous system, endothelial cells (ECs), cardiomyocytes, erythrocytes, hepatocytes and myocytes cells,
427 whereas epithelial and mesenchymal cells became more frequent (Fig. 7d-e). *Rbpj* deletion led to a 5
428 fold decrease in the frequency of ECs (Fig.7d, e), loss of expression of the arterial marker genes Gja5
429 and Gja4, and upregulation of the tip cell genes *Esm1, Kcne3, Apln* and *Cdkn1a* (Fig.7g,h). This
430 correlates with its essential role in the specification of arterial ECs and inhibition of tip ECs (Luo *et al.*,
431 2021; Pontes-Quero et al., 2019). $Rbpj^{KO}$ ECs also upregulated genes related with epithelia-to-
432 mesenchymal transition, glycolysis and angiogenesis and were less in cycle (Fig.7i). Analysis of other
433 cell types scRNAseq data revealed that *Rbpj* loss changes the relative frequency of specific cell types
434 clusters, suggesting an impact of this gene in their proliferation or differentiation. Indeed, different
435 genes and genetic pathways were deregulated after *Rbpj* deletion in the many cell types and clusters
436 identified (Fig. 7j-r and Sup. Fig. 7). This data provides an example how the combination of ratiometric
437 *iFlpMosaics* with scRNA-seq analysis can be very powerful to determine, in a high-throughput manner,
438 a gene cell-autonomous function in all cell types during development or in disease.

439

440 **Discussion**

441

442 Genetic mosaics are essential to understand a gene cell-autonomous function, and prevent confounding
443 effects frequently associated to classical whole animal or tissue-specific conditional genetics. With
444 inducible mosaic genetics, the mutant and wildtype cells share the same microenvironment and
445 developmental or physiological history, being the only difference between them the deleted gene. This
446 provides a much more accurate way to study and understand a gene cell-autonomous function during
447 tissue development, homeostasis or in disease.

448 We and others have observed that the transcriptional programs and phenotype of single mutant cells in
449 genetic mosaics, are often very different from the programs and phenotypes of single cells extracted
450 from a tissue in which that gene was deleted in most of the tissue cells (Hansen *et al.*, 2022). Performing
451 comparative omics of mutant and wildtype cells in genetic mosaics will more accurately reveal the true
452 gene molecular and cellular function. With classical genetics, the changes in the mutant tissue function
453 and its microenvironment can always impact the transcriptional program of the mutant cells in ways
454 that are unrelated with the original gene function or genetic program. As an example, if a gene impairs
455 vascular development or permeability, the entire surrounding tissue growth, function and paracrine
456 signals will be affected, and these in turn will influence the mutant cells phenotype. With genetic
457 mosaics, these effects are controlled for, because the wildtype and mutant cells used for comparison
458 share the same history and microenvironment.

459 The most frequently used methods to perform mosaic conditional genetics in mice, the most widely
460 used model in biomedical research, have several caveats. Genetic mosaics induced by CreERT2 are
461 easy to achieve, but are unreliable (Fernandez-Chacon *et al.*, 2019; Liu *et al.*, 2013; Schmidt-Supprian
462 and Rajewsky, 2007). These lack the co-induction of wildtype cells labelling for direct phenotypic
463 comparisons with the mutant cells. MADM is genetically very reliable, and has an internal control, but
464 is a cumbersome and inefficient method, providing no temporal resolution in the induction and genetic
465 analysis (Contreras *et al.*, 2021; Zong, 2014; Zong *et al.*, 2005).

466 The set of new genetic tools decribed here significantly improve on these two technologies. In contrast
467 to Cre-ERT2 genetics, *iFlpMosaics* provide clearly distinguishable and reliable fluorescent labels for
468 both mutant (Tomato) and wildtype (YFP) cells. The simultaneous and ratiometric induction of both
469 mutant and wildtype cells fluorescent labels at the same time, and in the same tissue, is very important,
470 since it provides a way to accurately measure and compare how these cells differ in their proliferation,
471 differentiation, migration or survival. We have shown that this can be done over short or long periods
472 of time. The fluorescent markers are easily detectable and quantifiable by both microscopic imaging or
473 FACS. In contrast to MADM, *iFlpMosaics* provide a high degree of inducibility, at any specific time
474 point and in any cell type, including quiescent cells present in adult mice, which will be very important
475 to model the etiology of diseases caused by sporadic somatic mutations. In addition, it is compatible
476 with all existent floxed alleles, being possible to mosaicly delete multiple floxed genes in cis, which
477 will be essential for genetic functional epistasis analysis, with single-cell resolution. With *iFlpMosaics,*
478 instead of only 1*,* up to 12 different multispectral barcodes for mutant cells and 4 for wildtype cells are
479 possible. This significantly higher spectral barcode diversity, and dual labelling (membrane and nuclei)
480 also significantly increases single cell and clonal resolution during a pulse-and-chase genetic
481 experiment.

482 In *iFlpMosaics* cells expressing MbTomato also express Cre, a recombinase shown before to be toxic
483 when expressed at high levels (Loonstra et al., 2001; Naiche and Papaioannou, 2007; Rashbrook et al.,
484 2022). However, we found that the expression of the *iFlpMosaic* alleles is relatively low, when
485 compared with previously published Cre-expressing lines (Fernandez-Chacon *et al.*, 2019). This can be
486 due to the different DNA elements used, and the presence of only one upstream insulator during Rosa26
487 targeting. It has been shown that the PGK-Neo cassette and the 2A peptide elements used in i*FlpMosaic*
488 alleles reduce the expression or translation efficiency (Ema et al., 2006; Pontes-Quero *et al.*, 2017;
489 Sharma et al., 2012). The absence of Cre toxicity was confirmed by the analysis of the relative ratio of
490 Tomato/YFP cells over long periods of time during development of many cell lineages *in vivo*. This
491 ratio was kept constant over time when in a wildtype genetic background.

492 Single cell biology during tissue development is highly heterogenous, and therefore is also
493 important to be able to reliably induce and analyse genetic mosaics of mutant and wildtype cells derived

494 from single progenitor cells and with a minimal ammount of false positives and false negatives. The
495 previously established MADM technology is ideal for this (Contreras *et al.*, 2021; Zong, 2014; Zong *et*
496 *al.*, 2005), but it lacks temporal inducibility and efficiency. With the new *iFlp/Dre*^{Progenitor} allele, we
497 were able to significantly increase the inducibility and precision of *iFlpMosaics*. The *iFlp/Dre*^{Progenitor}
498 allele FRT/Rox cassette, or genomic locus, is very sensitive to FlpOERT2/DreERT2 recombinases, and
499 results in a genetic expression cascade and delay in the expression of FlpO, that is very convenient to
500 generate different mutant and wildtype cells within the progeny of a single progenitor cell, something
501 only possible to achieve so far with MADM. The progeny cells will also permanently express the nuclei
502 marker H2B-V5 and the surface marker hCD2, ideal for FACS or quick magnetic isolation of the cells.
503 Integration of information arising from *in situ* single-cell lineage-tracing microscopy methods, with
504 information derived from new scOMICs and bioinformatic analysis methods, will be essential to establish the
505 biology of single-cell lineages with high detail and in a realiable and high-throughput manner. We showed
506 how the combination of *iFlpMosaics* with FACS or scRNA-seq analysis provide an easy way to analyse
507 in a high-througput manner the cell-autonomous function of any gene in all cell types, during
508 development, homeostasis or disease. Since the mosaics of mutant and wildtype cells can be induced in
509 less than 10% of the animal cells, they will not severely affect tissue or organ development/homeostasis,
510 allowing analysis of the transcriptional, epigenetic, proliferative or differentiation state of all mutant
511 cells in a mostly wildtype environment. This means that crossing a floxed gene with multiple
512 independent CreERT2 lines (one for each cell type), is no longer needed to understand its cell-
513 autonomous function. The ubiquituous and strongly expressed FlpOERT2 and DreERT2 lines generated
514 here allow induction of *iFlpMosaics* in all cell types, at both low or high frequencies. This enables
515 direct comparisons of the molecular and cellular phenotypes of mutant and wildtype cells extracted
516 from all tissues of an embryo or animal.
517 *iFlpMosaics* will greatly facilitate the induction and high-throughput analysis of somatic
518 genetic mosaics and turn possible the understanding how an individual or combinatorial set of genetic
519 mutations affect the biology of single cells during tissue development, regeneration or disease.
520
521
522
523 **Methods**
524
525 **Mice**
526
527 We generated and used Mus musculus with C57BL6 or C57BL6×129SV or B6CBAF1 genetic
528 backgrounds. All mice were backcrossed to C57Bl6 for a few generations. To generate mice for

529 analysis, we intercrossed mice with an age range between 7 and 30 weeks. We do not expect our data
530 to be influenced by mouse sex. The following mouse lines and alleles were used and interbred:
531 *Tg(Cdh5-CreERT2)* (Wang *et al.*, 2010), *Tg(iSuRe-Cre)* (Fernandez-Chacon *et al.*, 2019), *Notch1*$^{flox/flox}$
532 (Radtke et al., 1999), *Rbpj*$^{flox/flox}$ (Han et al., 2002), *Myc*$^{flox/flox}$ (de Alboran et al., 2001),
533 *Mycn*$^{flox/flox}$(Knoepfler et al., 2002), *Foxo1/3/4*$^{flox/flox}$(Paik et al., 2007), *Rosa26-EYFP (Srinivas et al.,*
534 *2001), Rosa26-iChr2-Mosaic* (Pontes-Quero *et al.*, 2017), Tg-*iMb2-Mosaic or iCre*$^{MYFP/Tomato/MTFP1}$
535 (Pontes-Quero *et al.*, 2017), *Gt(Rosa)26*$^{tm3(CAG-FlpOERT2)Ali}$(Lao *et al.*, 2012), *Gt(Rosa)26Sor*$^{tm14(CAG-LSL-}$
536 $^{tdTomato)Hze}$(Madisen et al., 2010) and *Apln-FlpO* (Luo et al., 2021). The following mouse lines were
537 produced in this study: *R26-iFlp*$^{MTomato-Cre/MYFP}$, *Tg-iFlp*$^{MTomato-H2B-GFP-Cre/MYFP-H2B-Cherry-FlpO}$, *Tg(INS-CAG-*
538 *FlpOERT2), Tg(INS-CAG-DreERT2), Tg(Cdh5-FlpOERT2), Tg(Cdh5-DreERT2), iFlp*^{Chromatin}*-Mosaic*
539 and *Tg-iFlp/Dre*^{Progenitor} .

540 *Tg-iFlp*$^{MTomato-H2B-GFP-Cre/MYFP-H2B-Cherry-FlpO}$, *Tg(INS-CAG-FlpOERT2), TgiFlp*^{Chromatin}*-Mosaic* and
541 *Tg-iFlp/Dre-Progenitor* mouse alleles were generated by standard DNA injection in mouse eggs and screening
542 of several transgenic founders as indicated in the main text or figures. The *R26-iFlp*$^{MTomato-Cre/MYFP}$ allele was
543 generated by CRISPR-assisted gene targeting in G4 ES cells of the Rosa26 locus using the guide
544 GACTGGAGTTGCAGATCACGA_GGG (IdT DNA) and a Donor DNA with the elements indicated
545 in Figure 1. Targeted ES cells were used for mice production. The *Tg(Cdh5-FlpOERT2) and Tg(Cdh5-*
546 *DreERT2)* lines were generated by CRISPR-Cas9-assisted gene targeting using mouse eggs of the
547 existing *Tg(Cdh5-CreERT2)* line (Wang et al., 2010) with the guide
548 AAGCTTATCGATACCGTCGA_CGG and a donor DNA containing either the Cdh5-FlpOERT2 or
549 Cdh5-DreERT2 sequences. *Tg(INS-CAG-DreERT2)* mice were generated by CRISPR-Cas9 using
550 guide RNAs (GATGTCGAACTGGCTCATGG_TGG and AACAGGCGGATCTGCGTACG_CGG)
551 targeting the existing FlpO sequence contained in the pre-screened *Tg(INS-CAG-FlpOERT2)* transgene,
552 and a donor DNA containing the CAG-DreERT2 sequence. Injections mixtures were composed by the
553 described crRNAs (IDT) and tracrRNA (IDT, catalog 1072533) at 0.305 microM and Cas9 nuclease
554 (Alt-R® S.p. HiFi Cas9 Nuclease V3, 100 µg, Catalog 1081060) at 20 ng/microL. Founders were
555 initially screened by PCR with the primers in Supplementary Table 1.

556 To induce CreERT2, FlpOERT2 or DreERT2 activity in adult mice, 1g tamoxifen (Sigma-
557 Aldrich, P5648_1G) were dissolved in 50ml corn oil (20 mg/ml tamoxifen) and aliquots stored at -20C.
558 From this stock solution, animals were given intraperitoneal injection of 50ul to 100ul (total dose of 1
559 to 2 mg tamoxifen per animal at 40 to 80mg/kg) as indicated in figures. To activate recombination in
560 pups, 4-hydroxytamoxifen (4-OHT) tamoxifen was injected at the indicated stages at a dose of 40 mg/kg
561 body weight. All mouse lines and primer sequences required to genotype these mice are provided in
562 Supplementary Table 1.

All mouse husbandry and experimentation was conducted using protocols approved by local animal ethics committees and authorities (Comunidad Autónoma de Madrid and Universidad Autónoma de Madrid CAM-PROEX 177/14, CAM-PROEX 167/17, CAM-PROEX 164.8/20 and PROEX 293.1/22). The mouse colonies (Mus musculus) were maintained in racks with individual ventilation cages according to current national legislation. Mice have dust/pathogen-free bedding, and sufficient nesting and environmental enrichment material for the development of species-specific behavior. All mice have 'ad libitum' access to food and water in environmental conditions of 45–65% relative humidity, temperatures of 21–24 °C, and a 12 h/12 h light/dark cycle. In addition, and to preserve animal welfare, mouse health is monitored with an animal health surveillance program, which follows FELASA recommendations for specific pathogen-free facilities.

Immunofluorescence on cryosections

Tissues were fixed for 2 h in 4% PFA in PBS. After three washes in PBS for 10 min each, organs were stored overnight in 30% sucrose (Sigma) in PBS. Organs were then embedded in OCT™ (Sakura) and frozen at -80°C. Cryosections (35□m□□were cut on a cryostat (Leica), washed three times for 10 min each in PBS, and blocked and permeabilized in PBS containing 10% donkey serum (Milipore), 10% fetal bovine serum (FBS), and 1% Triton X-100. Primary antibodies were diluted in blocking/permeabilization buffer and incubated overnight at 4°C. This step was followed by three 10 min washes in PBS and incubation for 2 h with conjugated secondary antibodies (1:200, Jackson Laboratories) and DAPI in PBS at room temperature. After three washes in PBS, sections were mounted with Fluoromount-G (SouthernBiotech). All antibodies used are listed in Supplementary Table 2.

586 **Wholemount Immunofluorescence of retinas**

587

588 For postnatal mouse retina immunostaining, eyes were collected and fixed in cold 4% PFA in PBS for
589 10 minutes. After fixed for 15 minutes more at room temperature. After washed once in PBS and kept
590 on ice. After microdissection with spring scissors (FST), retinas were fixed in 4% PFA for an additional
591 45 min at room temperature, followed by two PBS washes of 10 min each. Retinas were blocked and
592 permeabilized with PBTS buffer (0.3% Triton X-100, 3% fetal bovine serum (FBS) and 3% donkey
593 serum) for 1 h. Samples were then incubated overnight at 4 °C in Biotinylated isolectinB4 (Vector Labs,
594 B-1205, diluted 1:50) and primary antibodies (Supplementary Table 2) diluted in PBTS buffer. After
595 five washes (20 min each) in PBTS buffer diluted 1:2, samples were incubated for 2 h at room
596 temperature with Alexa conjugated secondary antibodies (Supplementary Table 2). After three washes
597 of 30 min each in PBTS buffer (diluted 1:2), and two washes of 15 min each in PBS, retinas were
598 mounted with Fluoromount-G (SouthernBiotech).

599

600 **In vivo EdU labelling and EC proliferation detection**

601

602 To detect EC proliferation in postnatal livers and pancreas, 20 μg g^{-1} body weight EdU
603 (Invitrogen, A10044) was injected intraperitoneally into P1, P7 or P20 mice 4h before dissection. Livers
604 and pancreas were fixed in PFA4% and processed for OCT cryoblocks and sections as mentioned above.
605 EdU signals were detected with the Click-it EdU Alexa Fluor 647 or 488 Imaging Kit (Invitrogen,
606 C10340 or C10337). In brief, after all other primary and secondary antibody incubations, samples were
607 washed according to the immunofluorescence staining procedure and then incubated with Click-iT EdU
608 reaction cocktail for 40 min, followed by DAPI counterstaining.

609 **Image acquisition and analysis**

610

611 Immunostained organ sections or whole mount retinas were imaged at high resolution with a
612 SP8 Navigator confocal microscopes fitted with 10x, 20x, or 40x objectives for confocal scanning.
613 Individual fields or tiles of large areas were acquired. All images shown are representative of the results
614 obtained for each group and experiment. Animals were dissected and processed under exactly the same
615 conditions. Comparisons of phenotypes or signal intensity were made with pictures obtained using the
616 same laser excitation and confocal scanner detection settings. Fiji/ImageJ was used to threshold, select,
617 and quantify objects in confocal micrographs. Both manual and automatic ImageJ public plugins and
618 customed Fiji macros were used for quantification.

619

620 **Fluorescence activated flow cytometry and sorting**

621

622 Embryonic, postnatal or adult tissues were first dissociated before fluorescence activated flow
623 cytometry or sorting (FC or FACS). Embryonic tissues were dissociated using Miltenyi Biotec Tissue
624 Dissociation Kit 2 following the instructions (130-110-203). Postnatal and adult mouse tissues were
625 first digested for 20min at 37ºC with 2.5 mg/ml collagenase type I (Thermofisher), 2.5 mg/ml dispase
626 II (Thermofisher) and 50 **u**g/ml DNAseI (Roche).

627 Dissociated samples were filtered through a 70-µm cell strainer, and cells were centrifuged
628 (400g, 4°C for 5 min). Cell pellets were gently resuspended in blood lysis buffer (0.15 M NH_4Cl,
629 0.01M $KHCO_3$ and 0.01 M EDTA in distilled water) and incubated for 10 minutes on ice to remove
630 erythroid cells. Cells were centrifuged (400g at, 4°C for 5 min), and cell pellets were gently
631 resuspended in blocking solution (DPBS without Ca^{2+} or Mg^{2+} and containing 3% dialyzed FBS
632 (Termofisher)) and incubated at 4ºC with shaking for 20min. Cells were centrifuged (300g at 4°C for
633 5 min), resuspended and incubated for 30min at 4C with APC rat-anti-mouse CD31 (BD Pharmigen,
634 551262, 1:200) and APC-CY7 anti-CD45 (BD Pharmigen, 1:200). Cells were then centrifuged (400g,
635 4°C for 5 min), resuspended and washed in DPBS without Ca^{2+} or Mg^{2+} and centrifuged again, and
636 cell pellets were resuspended in blocking solution. Cells were kept on ice until used for FC or FACS.
637 DAPI (5 mg/ml) was added to the cells immediately before analysis. Cells were routinely analysed in
638 Fortressa or sorted in a FACS Aria Cell Sorter (BD Biosciences). BD FACS Diva V8.0.1 and Flow
639 JO v10 was utilized for FACS data collection and analysis.

640

641 **Cells isolation for transcriptomic analysis**

642

643 For qRT-PCR analysis, approximately 20.000 DAPI negative Tomato+ or YFP+ cells from dissociated
644 tissues were sorted directly to buffer RLT (RNAeasy Micro kit - Qiagen) and RNA extracted according
645 to the manufacturer instructions and stored at -80°C. This RNA was later used for qRT-PCR or RNAseq
646 analysis. For quantitative real time PCR (qRT-PCR), total RNA was retrotranscribed with the High
647 Capacity cDNA Reverse Transcription Kit with RNase Inhibitor (Thermo fisher, 4368814). cDNA was
648 preamplified with Taqman PreAmp Master Mix containing a Taqman Assay-based pre-amplification
649 pool containing a mix of the Taqman assays indicated in Supplementary Table 3. Preamplified cDNA
650 was used for qRT-PCR with the same gene specific Taqman Assays and Taqman Universal Master Mix
651 in a AB7900 thermocycler (Applied Biosystems). AB7900 software was used to retrieve and analyse
652 data.

653 For RNA-seq analysis, embryos were dissociated using Miltenyi Biotec Multi Tissue Dissociation Kit
654 2 following the instructions. A volume of 1,2ml of dissociation solution was used per embryo inside a
655 2ml round bottom tube. Following a 5 minutes incubation in a 37C water bath, tubes were put inside a
656 pre-warmed 50ml falcon and incubated for 25 minutes in the MACSmix Tube Rotor. After cells were
657 resuspended with a Gilson P1000 pipet for 30 times. Starting slow and increasing speed gradually. To
658 the 1.2ml of cells, 3ml of sorting buffer (10% FBS in DPBS -Ca2-Mg2-) was added and this solution
659 transferred to a 5ml syringe. This volume was pressed slowly through a small 70 microns strainer to
660 remove clumps. Each embryo gave around 30 million cells at this stage. Cells suspensions were spinned
661 at 400g for 6 minutes. Pellet was detached and ressuspended in 300ul sorting buffer containing DAPI.
662 DAPI negative, single, and live Tomato+ and YFP+ cells were sorted to eppendorf tubes containing
663 300ul of Sorting buffer. 66k Tomato+ and 30k YFP+ cells were sorted using a 100um Nozzle, 20 PSI
664 and high purity scale and low flow rate (1) to preserve cell viability and decrease contamination. At the
665 end sorted cells were spinned at 500g for 5min, and ressuspended in 30-40ul Cell Capture Buffer (DPBS
666 (-)Ca2+ (-)Mg2+ with 0.04%BSA). After counting cells in Countess III, two independent 10x genomics
667 ports were loaded with either 16k Tomato+ cells (90% vaibility) or 16k YFP+ cells (88% viability).

668

669 **Next Generation Sequencing sample and library preparation**

670

671 Next Generation Sequencing (NGS) experiments were performed in the Genomics Unit at
672 CNIC. For scRNA-seq experiments, single cells were encapsulated into emulsion droplets using the
673 Chromium Controller (10x Genomics). scRNA-seq libraries were prepared according to the
674 manufacturer's instructions. The aimed target cell recovery for each port was 10000 cells. Generated
675 libraries were sequenced on a HiSeq4000 or NextSeq2000 (Illumina).

676

677 **Transcriptomic data analysis**

678

679 Transcriptomic data were analyzed by the CNIC Bioinformatics Unit, Alvaro Regano and Irene
680 Garcia.

681 The following pipeline was followed for scRNA-seq data processing and *in silico* cell type selection.
682 For alignment and quantification of gene expression, the reference transcriptome was built using mouse
683 genome GRCm39 and Ensembl gene build v109 (https://ftp.ensembl.org/pub/release-
684 109/fasta/mus_musculus). The WPRE-sv40pa sequences expressed in the Tomato+ and YFP+ samples
685 were added to the reference. Gene metadata were obtained from the corresponding Ensembl BioMart
686 archive. Reads from transcripts were processed, aligned and quantified using the Cell Ranger v6.1.2

687 pipeline. Single-cell analysis was based on Seurat (Hao et al., 2021) and DoubletFinder R packages.
688 Low-quality cells were filtered out using the following criteria: total counts, >1,000 and <55,000; genes
689 detected, >500 and <7,500; mitochondrial transcripts content, <15%; hemoglobin transcripts, <1%;
690 ribosomal transcripts, <35. Counts were log-normalized and scaled, followed by principal component
691 analysis (PCA) and clustering using the shared nearest-neighbors algorithm and Louvain clustering
692 (settings as defaults except for the 2,000 most variable genes, 24 principal components, and a resolution
693 of 0.35). Clusters and cells were classified based on the SingleR method (Aran et al., 2019) using
694 Blueprint ENCODE, the Human Primary Cell Atlas cell-type profile collection and a scRNASeq mouse
695 dataset from the celldex package. This identification was used to predefine the different cell types
696 present in the dataset for the analysis. Doublets were removed using DoubletFinder, using a first
697 annotation with 24 PCs, 0.25 pN and a pK of 0.05, and the second one with 10 PCs, pN0.25 and pK
698 0.05. Cells classified as Singlets were preserved. Singlets were then reclustered using 19 PCAs and a
699 clustering resolution of 0.35. Manual curation of the identified clusters was applied to confirm and
700 finetune the identity of the clusters based on scRNAseq bibliography.

701

702 **Copy number assay and qRT-PCR**

703 To identify the number of copies for *FlpO or Cre* expressing cassettes after transgenesis, the genomic
704 DNA was extracted from mouse tails biopsies using the phenol chloroform protocol as follows:
705 overnight digestion in 500 µL of proteinase K buffer (10 mM Tris-HCl [pH 8.0], 100 mM NaCl, 10
706 mM EDTA [pH 8.0], 0.5% sodium dodecyl sulfate, 0.25 mg/mL proteinase K) with occasional
707 vortexing. Following digestion, 250 µL of phenol and 250 µL of chloroform was added followed by
708 vigorous vortexing to ensure thorough mixing of phenol:chloroform with the sample. Samples were
709 immediately subjected to microcentrifugation at maximum speed for 5 minutes to allow separation of
710 the aqueous and organic layers. 300 µl of the aqueous top layer was removed with a 200 µl pipet, paying
711 careful attention to avoid the interface. To the 300µl of solution we added 1:10 (30µl) of sodium acetate
712 (NaAc) 3M and 2.5x (825 µl) of EtOH 100%. Then the tubes were shaken up and down 10 times to
713 precipitate the DNA. Samples were spin down at maximum speed for at least 45 minutes at 4ºC. Then
714 supernatant was removed and immediately after we added 500 µl of 70% ethanol and samples were
715 pelleted by centrifuging at max speed for 5 minutes. Pellets were re-suspended in 100µl of TE solution
716 (Tris 10mM pH=8 and EDTA 0.1mM pH=8) overnight. Next day, DNA concentrations were measured
717 in nanodrop and diluted at a final concentration of 10ng/µl.

718 For the copy number assays we performed qRT-PCR with TaqMan Universal Master Mix (TaqMan,
719 4440049) and the following probes: Tert TaqMan Copy Number Reference Assay (TaqMan probe,
720 4458369). A probe and a set of amplifying primers designed in the lab and synthetized by iDT to detect

721 the *FlpO* gene (FlpO-qPCR-F: CTGTACCAGTTCCTGTTCCTG, FlpO-qPCR-R:
722 CTTGTCTTGGTCTCGGTCAC) and qPCR FlpO Probe : TCTTGATGTCGCTGAACCTGCCG,
723 fluorophore FAM). To detect the *Cre* gene: a pre-designed Cre Assay was used (Mr00635245_cn ,
724 ThermoFisher).

725

726 With the Tert probe as a reference, the relative number of copies of the genes of interest were
727 inferred. Both Tert and FlpO/Cre probes were combined in the same reaction since they emitted two
728 different fluorophores, FAM and VIC. The qRT-PCR reactions were run in an AB7900 thermocycler
729 (Applied Biosystems).

730

731 **Statistical analysis and Reproducibility**

732

733 All bar graphs show mean ± s.d. Experiments were repeated with independent animals.
734 Comparisons between two groups of samples with a Gaussian distribution were carried out by unpaired
735 two-tailed Student *t*-test. Comparisons among more than two groups were made by one-way ANOVA
736 followed by multiple comparison tests. All calculations were done in Excel, and final datapoints were
737 analyzed and represented with GraphPad Prism. No randomization or blinding was used, and animals
738 or tissues were selected for analysis based on their genotype, the detected Cre/FlpO/Dre-dependent
739 recombination frequency, and the quality of multiplex immunostaining. Sample sizes were chosen
740 according to the observed statistical variation and published protocols.

741

742 **Data availability**

743

744 RNA-seq data can be viewed at the Gene Expression Omnibus (GEO) under accession numbers
745 GSEXXXX. Instructions and code to reproduce all scRNA-seq results can be found at
746 https://github.com/RuiBenedito/Benedito_Lab. Unprocessed original photos of the data are available
747 upon request. All other data supporting the findings in this study are included in the main article and
748 associated files.

749

750 **Acknowledgments**

751

752 Research in the Benedito laboratory was supported by the European Research Council (ERC) Starting
753 Grants AngioGenesHD (638028) and Consolidator Grant AngioUnrestUHD (101001814), the
754 Ministerio de Ciencia y Innovación (SAF2017-89299-P and PID2020-120252RB-I00) and “la Caixa”

Banking Foundation (project code HR19-00120 and HR22-00316 AngioHeart). The CNIC is supported by the Instituto de Salud Carlos III (ISCIII), the Ministerio de Ciencia e Innovación (MCIN) and the Pro CNIC Foundation, and is a Severo Ochoa Center of Excellence (grant CEX2020-001041-S funded by MICIN/AEI/10.13039/501100011033).

Microscopy experiments were performed at Microscopy and Dynamic Image Unit, CNIC, ICTS-ReDib, co-funded by MCIN/AEI /10.13039/501100011033 and FEDER "Una manera de hacer Europa" (#ICTS-2018-04-CNIC-16).

I.G.-G. was supported by a PhD fellowship from Fundación La Caixa (CX-SO-16-1). A.R. was supported by The Youth Employment Initiative (YEI) PEJD-2019-PRE/BMD-16990. L.G.-O. was supported by the Spanish Ministry of Economy and Competitiveness (PRE2018-085283).

We thank S. Bartlett (CNIC) for English editing; the members of the CNIC Transgenesis, Microscopy, Genomics, Citometry and Bioinformatic units. We also thank F. Alt (Boston Children's Hospital - Harvard Medical School), T. Honjo (Kyoto University Institute for Advanced Studies), F. Radtke (Swiss Institute for Experimental Cancer Research), R. H. Adams (Max Planck Institute for Molecular Biomedicine) and R. De Pinho (MD Anderson Cancer Center) for sharing the *Myc* ^{floxed}, *Rbpj* ^{floxed}, *Notch1*^{floxed}, *Cdh5(PAC)-creERT and Foxos1/3/4*^{floxed} mice respectively.

Author contributions statement

I.G-G. and R.B. designed most of the experiments, interpreted results, assembled figures and wrote the manuscript. R.B. designed all DNA vectors. I.G-G. did most of the DNA engineering (cloning), CRISPR-Cas9 genome targeting and executed the large majority of the animal experiments, confocal microscopy and FACS analysis. Mice were generated by the CNIC transgenesis unit. S.G. developed new methods for *iFlpMosaics* induction, tissues immunostaining and microscopy multispectral imaging. L.G-O, W.L., I.Z. and M.F-C. performed some animals experiments, FACS, histology and confocal imaging. I.G-G and A.R analysed scRNA-seq data. A.R. cloned and validated the *iFlp/Dre*^{Progenitor} allele. S.F.R. did image quantifications in Fiji, graphpad, text and figures editing and figures assembly. M.L, M.S.S-M, A.G.-C, F.L. and V.C-G gave general technical assistance with experiments and genotyped the mouse colonies. All authors approved the final version of the manuscript.

Competing interests statement

The authors declare no competing interests.

787 **Figure legends:**

788 **Figure 1: *iFlpMosaics* allow efficient and ratiometric labelling of mutant and wildtype cells. a,**
789 Schematic showing a standard Cre-reporter and how it may recombine and label cells without any
790 floxed gene (G) deleted (false positives). Non-recombined cells can also have the gene deleted (false
791 negatives). **b,** Different recombination efficiencies of several Cre-reporters, despite all localizing to the
792 *Rosa26* locus and having a similar genetic distance between LoxP sites. **c,d,** Cre-reporters only
793 accurately report recombination of themselves, not of other floxed alleles (reporters), particularly at low
794 doses of tamoxifen. **e,** Schematic of the novel R26-*iFlp*$^{MTomato\text{-}Cre/MYFP}$ allele, where Flpo/FlpOERT2-
795 induced recombination of the mutually exclusive FRTF3 and FT5T2 sites leads to one of two possible
796 outcomes (see also Sup. Fig. 1x). Cells expressing MTomato and Cre (mutant) or MYFP (wildtype).
797 The induction leads to the ratiometric proportion of around 65%MTom+:35%MYFP+. **f**, Tg-*iFlp*$^{MTomato\text{-}}$
798 $^{H2B\text{-}GFP\text{-}Cre/MYFP\text{-}H2B\text{-}Cherry\text{-}FlpO}$ allele and confocal micrographs showing the full spectral separation of the
799 4 fluorescent labels expressed in mutant and wildtype cells. **g,** In a wildtype background, the initial
800 ratiometric proportions between MTomato+ cells and MYFP+ cells are maintained through
801 embryogenesis to postnatal stages, indicating lack of toxicity of Cre in MTomato+ cells. **h**, Comparison
802 of MTomato intensity and Cre expression in cells of R26-*iFlp*$^{MTomato\text{-}Cre/MYFP}$ and Tg(*iSure-Cre*) mice. **i,**
803 Efficient recombination of the Cre-reporter *Rosa26*$^{\text{-}LSL\text{-}YFP}$ in MTomato+ cells (white arrowheads) after
804 induction of the R26-*iFlp*$^{MTomato\text{-}Cre/MYFP}$ allele by *Apln-FlpO*. Few cells are false positives (red arrows).
805 FACS data of the same animals livers and related chart. **j,** Combination of the *iFlp*$^{MTomato\text{-}Cre/MYFP}$ allele
806 with other floxed genes leads to very significant deletion of these in MTomato+ cells. **k,** Induction of
807 *iFlp*$^{MTomato\text{-}Cre/MYFP}$ in the *Rbpj* floxed background, a gene known to be essential for arterial development,
808 results in only 3.5% Tomato-2A-Cre+ cells in arteries (A), versus 96% in veins (v) and capillaries. Data
809 are presented as mean values +/- SD. For statistics see Source Data File 1. Scale bars are 50µm.
810

811 **Figure2: Generation of ubiquitous and tissue-specific FlpoERT2 mouse lines. a,** Recombination of
812 the *iFlp*$^{MTomato\text{-}Cre/MYP}$ mosaic mouse lines induced by the published *R26*$^{CAG\text{-}FlpoERT2}$, led to reduced
813 recombination efficiency at embryonic and postnatal stages and in adult organs. **b,** Schematic of novel
814 *Tg(Ins-CAG-FlpoERT2*) alleles containing optimized DNA elements in order to enhance FlpOERT2
815 expression. **c,** Comparison of FlpO copy number by genomic DNA qRT-PCR. **d-g** Comparison by
816 FACS and histology of the recombination efficiency among the different FlpOERT2-expressing mouse
817 lines/founders at embryonic, postnatal and adult stages. Fold change is indicated for the most
818 significant. **h,** Schematic of the generation of novel endothelial-specific *Cdh5-FlpoERT2*-expressing
819 mouse lines from the published Cdh5-CreERT2 mouse line by Crispr/Cas9 targeting. **i,** Comparison of
820 FlpO and Cre copy number by genomic DNA qRT-PCR. **j,** Recombination efficiency of Founder #1 of
821 the newly generated *Tg(Cdh5-FlpoERT2)* mouse line in embryonic, postnatal and adult tissues. Data
822 are presented as mean values +/- SD. For statistics see Source Data File 1. Scale bars are 100µm.

823 **Figure3: Ratiometric iFlpMosaics allow the high-throughput assessment of a gene cell-**
824 **autonomous function. a,b,** *iFlp*$^{MTomato\text{-}Cre/MYP}$ mosaics were induced with *Apln-FlpO* (recombines
825 endothelial and derived hematopoietic cells at E9.5) in a control/wildtype and Myc floxed background,
826 and tissues analysed at P7. FACS data of CD31+ (ECs) and CD45+ (Blood) cells shows that *Myc*
827 deletion (in MTomato+ cells) leads to a competitive disadvantage, especially in blood cells. Absolute
828 fold change indicated in red. **c,** When *iFlp*$^{MTomato\text{-}Cre/MYFP}$ mosaics are induced in most embryonic cells
829 with *ACTB:FlpE*, analysis of other organs cell types (CD31-CD45-) reveals that *Myc* is necessary for
830 liver, but not lung or heart cells development. **d,** *iFlp*$^{MTomato\text{-}Cre/MYP}$ mosaics were combined with *Tg(Ins-*
831 *CAG-FlpOERT2)* on a control/wildtype and *Foxo1/3/4* floxed background and tamoxifen injected at P1
832 to induce recombination in all cell types. Liver, lung and heart cells were analysed at P15 by FACS.
833 *Foxo1/3/4* deletion (in MTomato+ cells) increased the proliferation of heart cells, but not liver or lung
834 cells. **e,** Representative confocal micrographs of control and *Foxo1/3/4* mosaic P6 and P15 retinas of
835 animals induced at P1. Chart with ratiometric analysis of retina immunostainings for Tomato, YFP and
836 ERG (labels ECs nuclei) showing that *Foxo1/3/4*^{KO} ECs have a competitive advantage. Data are
837 presented as mean values +/- SD. For statistics see Source Data File 1. Scale bars are 100µm.
838
839 **Figure 4: Combining *iFlp-Mosaic* with *iFlp*^{Chromatin} for higher single-cell clonal resolution. a,**
840 Representative confocal micrograph of P20 liver sections of mice carrying the *Tg(Ins-CAG-FlpoERT2),*
841 *iFlp*$^{MTomato\text{-}Cre/MYFP}$ and *Rosa26-iChr2-Mosaic (iCre*$^{H2B\text{-}Cherry/GFP/Cerulean}$) alleles. Combination of these
842 membrane and nuclear reporter alleles allow up to 3 different mutant and 1 wildtype cell barcodes
843 (labelling). Note that binucleated (2x2n) or polyploid (4n) hepatocytes can have more multispectral
844 barcodes. **b,** Representative confocal micrograph of a P7 retina from an animal containing the *Tg(Ins-*
845 *CAG-FlpOERT2)* and the new *iFlp*^{Chromatin} nuclear reporter allele induced at P1 with 4-OHT. Bar shows
846 ratiometric frequency of each nuclear/H2B+ fluorescent marker. **c,** Representative confocal micrograph
847 of the indicated adult organ sections of animals carrying the *iFlp*^{Chromatin} and *Tg(Ins-CAG-FlpoERT2)*
848 alleles. Mononucleated diploid cells (kidney and lung) express only 1 of 3 possible nuclei/chromatin
849 markers, while multinucleated or polyploid cells (hepatocytes and cardiomyocytes) can express a
850 combination of 2 or 3 possible markers (6 possible chromatin barcodes in total). **d,** Recombination and
851 cell barcoding possibilities in animals carrying the indicated alleles. A representative P6 retina confocal
852 micrograph showing that both wildtype and mutant cells can be labelled in 4 different ways, which
853 significantly increases single cell clonal resolution. On the right is shown an example of how a Fiji
854 image analysis script automatically detects, segments, and pseudocolor the nuclei of dual-labelled
855 (nuclei and membrane) cells. **e,** Recombination and diploid cell barcoding possibilities in animals
856 carrying the indicated alleles. A representative confocal micrograph of an adult liver showing that mutant
857 hepatocytes can be labelled with up to 16 different fluorescent barcodes, depending on whether these are
858 mononucleated/diploid or multinucleated/polyploid. Also wildtype hepatocytes can have up to 8 different
859 fluorescent barcodes (only 6 shown). Scale bars are 100µm.

860

861 **Figure 5: High-resolution *iFlpMosaics* reveals the impact of genetic mutations in single cell clonal**
862 **dynamics. a,** Quantification of Ki67+ (in cycle) or EdU+ (S-phase) cells in P1, P7 and P20 livers. **b,**
863 Schematic of the indicated alleles combined in a single animal and how they can be used to fluorescently
864 barcode and track single mutant and wildtype cells clonal expansion from P1 to P20. Representative
865 confocal micrographs of P20 livers (from animals induced with 4-OHT at P1) with different
866 recombination frequencies are shown (see also Sup. Fig. 5). **c,** Recombination and fluorescent
867 barcoding density did not affect the clonal quantification. **d,** Liver weight increases 2.9 fold from P1
868 and P20. **e,** Quantification of MYFP+ (Myc^{WT}) and MTomato+ (Myc^{KO}) clone size frequency showing
869 that Myc^{KO} hepatocytes divide less. **f,** Chart depicting the normalized expansion of Myc^{WT} and Myc^{KO}
870 hepatocytes over the same period of 20 days. **g,** Representative confocal micrographs of P20 pancreas
871 from control and *Myc floxed* mice having the indicated *iFlpMosaic* alleles. Right panels correspond to
872 inverted LUT images depicting the clones mapping (by Fiji image analysis scripts) according to their
873 dual color code. **h,** Quantification of MYFP+ (Myc^{WT}) and MTomato+ (Myc^{KO}) clone size frequency
874 showing that Myc^{KO} pancreatic cells divide less. **i,** Chart depicting the normalized expansion of Myc^{WT}
875 and Myc^{KO} pancreatic cells over the same period of 20 days. **j,** Log2 ratio between Tom+ and YFP+
876 cells in control and *Myc floxed* pancreas showing a 3.7 fold loss of MTomato+ (Myc^{KO}) cells over 20
877 days. **k,** Representative confocal micrographs of adult livers from control and *Myc floxed* mice having
878 the indicated *iFlpMosaic and* $iCre^{Mb2\text{-}Mosaic}$ alleles induced 14 days before tissue collection. Right panels
879 correspond to automatic mapping of clones, using Fiji image analysis scripts, according to their
880 fluorescent barcode. Note the loss of MTomato+ cells in the Myc floxed background. **l,** Clone size
881 showing that wildtype hepatocytes rarely divide or expand over a period of 2 weeks. **m,** Quantification
882 of wildtype MYFP+ and MTomato+ hepatocyte clone frequency reveals no impact of Cre expression
883 in MTomato+ cells. Note the difference between diploid, mononucleated, polynucleated and polyploid
884 cells. **n,** Quantification of the percentage of YFP+ and Tomato+ clones that are proliferative (composed
885 by more than 1 cell) and non-proliferative. No major difference observed between both wildtype
886 populations. **o,** Log2 ratio of the Tom+ and YFP+ cells frequency in control and adult *Myc floxed* livers,
887 showing that a big fraction of Myc^{KO} cells are lost over 2 weeks. **p,** Among the surviving Myc^{KO} cells,
888 the frequency of non-proliferative binucleated cells increases and the frequency of proliferative
889 mononucleated cells decreases. **q,** Quantification of the percentage of YFP+ (Myc^{WT}) and Tomato+
890 (Myc^{KO}) clones that are proliferative and non-proliferative. Loss of *Myc* reduces the frequency of
891 proliferative clones.

892

893 **Figure 6: *iFlp/*$Dre^{Progenitor}$ enables the induction of genetic mosaics in the progeny of single cells.**
894 **a,** Schematic of the *iFlp/*$Dre^{Progenitor}$ DNA construct used to generate mice by transgenesis. **b**,

895 CRISPR-Cas9 assisted targeting of the *iFlp/Dre*^{Progenitor} donor DNA on an existing *Tg(Ins-CAG-*
896 *FlpOERT2)*^{F4} multicopy allele. **c,** Generation of *Tg(Ins-CAG-DreERT2)* by CRISPR-Cas9 mediated
897 replacement of FlpO by Dre in the existing *Tg(Ins-CAG-FlpOERT2)*^{F4} allele. **d**, Schematic of the
898 genetic cascade induced in animals containing the indicated alleles. After tamoxifen induction of
899 FlpOERT2 or DreERT2, the *iFlp/Dre*^{Progenitor} allele is recombined driving expression of the nuclei
900 marker H2B-V5, the surface marker truncated human CD2 (hCD2) and FlpO. FlpO is a relatively
901 weak recombinase, that needs to be expressed and accumulate in the cell before it recombines the
902 *iFlp*$^{MTomato\text{-}Cre/MYFP}$ allele. This delay results in recombination in the progeny of a single progenitor cell.
903 **e**,**f**, In animals lacking the *iFlp/Dre*^{Progenitor} allele, most single cell derived clones are formed by only
904 one type of cell (MTomato+ or MYFP+). With the *iFlp/Dre*^{Progenitor} allele is possible to induce clones
905 formed by mutant (MTomato+) and wildtype (MYFP+) cells derived from single progenitor cells (see
906 also Sup. Fig. 6). **g**, Retinas confocal micrographs showing that the *iFlp/Dre*^{Progenitor} allele increases
907 significantly the frequency of recombination of the *iFlp*$^{MTomato\text{-}Cre/MYFP}$ allele (induced at P3 and
908 collected at P7), enabling high frequency genetic mosaics with the weaker *Cdh5-FlpOERT2* line
909 (expressed only in Cdh5+ ECs). H2B-V5 labels the nuclei of cells recombining/expressing the
910 *iFlp/Dre*^{Progenitor} allele. **h**, FACS plots showing that the *iFlp/Dre*^{Progenitor} allele increases significantly
911 the frequency of recombination of the *iFlp*$^{MTomato\text{-}Cre/MYFP}$ allele when combined with the *Tg(Ins-CAG-*
912 *FlpOERT2)* allele.
913 **i**, Retinas confocal micrographs showing that when the new *Tg(Ins-CAG-DreERT2)* line is combined
914 with the *iFlp/Dre*^{Progenitor} allele, recombination of the *iFlp*$^{MTomato\text{-}Cre/MYFP}$ allele is also much more
915 frequent. H2B-V5 labels the nuclei of cells recombining/expressing the *iFlp/Dre*^{Progenitor} allele.
916
917 **Figure 7 : Combining single cell RNA-seq with ratiometric *iFlp*^{Mosaics} to uncover cell-autonomous**
918 **gene function. a,** Schematic of the induction of embryos having the indicated alleles at E9.5 and
919 collection of cells at E13.5 by FACS for scRNA-seq. **b**, Umaps showing the spatial distribution of the
920 *Rbpj*^{KO} (MTomato+) and *Rbpj*^{Wt} (MYFP+) cells and the different clusters they form. On the right, dot
921 plot showing the top markers used for the identification of the major cell types. **c**, Dot plot showing the
922 frequency and amplitude of expression for *Rbpj,* the canonical Notch target *Hes1*, and the G2/M phase
923 (proliferation) marker *MKi67* among wildtype (MYFP+) and mutant (MTomato-2A-Cre+) cells. Note
924 that *Rbpj* deletion only removes exons 6 and 7, leaving the 3´mRNA intact. However, this truncated
925 mRNA is less stable and less detectable after deletion. **d**,**e**, Histobars and Umap showing that mosaic
926 deletion of *Rbpj* (MTomato+ cells) changes the relative proportion of different cell types. **f-r**, Umaps
927 with the cell-type specific subclusters, top deregulated marker genes, and gene set enrichment analysis
928 charts showing how *Rbpj* deletion changes the frequency, differentiation and biology of the indicated
929 cell types.
930

931 **Supplementary Figure 1: *iFlpMosaics* are not toxic or leaky.**

932 **a, b,** Schematic of the novel Rosa26-*iFlp*$^{MTomato\text{-}Cre/MYFP}$ and Tg-*iFlp*$^{MTomato\text{-}H2B\text{-}GFP\text{-}Cre/MYFP\text{-}H2B\text{-}Cherry\text{-}FlpO}$
933 alleles, the genetic distances between the FRT sites pairs (mutually exclusive), and expected outcomes
934 after FlpO/FlpOERT2 recombination. **c, d** Mouse ES cells used to generate Rosa26-*iFlp*$^{MTomato\text{-}Cre/MYFP}$
935 mice were transfected with FlpO expressing plasmids, and analysed by confocal microscopy or FACS
936 3 days after. **e-g**, Frequency of recombination/expression detected in ES cells and ECs derived from
937 embryoid bodies (EBs) by microscopy. **h**, Relative frequency of MTomato-2A-Cre+ and MYFP+
938 cells does not change over time in both ES cells (in vitro) and in blood (in vivo), showing that the
939 permanent expression of Cre is not toxic to the cells. **i**, Combination of the standard *Rosa26-LSL-YFP*
940 allele with *iFlpMosaics* alleles allow determination of FlpO versus Cre-dependent leakiness by FACS
941 analysis of adult organs. FlpO leakiness was not detected (0% Tomato+ cells), and Cre-non-self-
942 leakiness (only detectable with the additional *Rosa26-LSL-YFP* allele) was only observed in a very
943 small fraction of cells from animals carrying the Tg-*iFlp*$^{MTomato\text{-}H2B\text{-}GFP\text{-}Cre/MYFP\text{-}H2B\text{-}Cherry\text{-}FlpO}$ allele. Not
944 in animals having the Rosa26-*iFlp*$^{MTomato\text{-}Cre/MYFP}$ allele.

945 **Supplementary Figure 2: Validation of *iFlpMosaics* for ratiometric quantitative gene function**
946 **analysis. a,** Representative confocal micrograph of P6 retinas of *Rbpj floxed* mice carrying the
947 *iFlp*$^{MTomato\text{-}Cre/MYFP}$ and *Apln-FlpO* alleles. *Apln* is an X-chromosome gene (mosaicly expressed in
948 females), expressed at the angiogenic front of growing vessels, recombining ECs that later form the
949 entire vasculature. It also recombines non-endothelial (ERG negative) cells in the retina. Right panel
950 showing ERG signal segmentation (EC nuclei), with nuclei belonging to Tomato+ (*Rbpj*^{KO}) cells or
951 YFP+ (*Rbpj*^{WT}) cells outlined in red or green, respectively. Grey nuclei are of ERG+ objects of non-
952 recombined cells. Dashed white lines show limits of leading edge (LE), angiogenic front (AF) and
953 mature area (MA). Chart depicting the log2 of the ratio between Tomato+ and YFP+ ECs in each of the
954 retinal regions, highlighting the enrichment of *Rbpj*^{KO} cells in the LE and AF, suggesting a role for this
955 gene in cell migration. **b,** Representative confocal micrograph of P6 retinas of *Rbpj floxed* mice carrying
956 the *iFlp*$^{MTomato\text{-}H2BGFP\text{-}Cre/MYFP\text{-}H2BCherry}$ and *Apln-FlpO* alleles, which also allows the nuclear labelling of
957 *Rbpj*^{KO} (H2B-GFP+) and *Rbpj*^{Wt} (H2B-Cherry+) cells, which is more convenient for cell object
958 segmentation and quantification of nuclear-specific proteins, such as the proliferation and cell cycle
959 arrest markers Ki67 and p21. Scale bars 150µm.

960

961 **Supplementary Figure 3: Comparative analysis of recombination efficiency of FlpOERT2 mouse**
962 **lines. a-d,** Representative FACs plots of different adult organs showing YFP+ and Tomato+ cell
963 frequency obtained from mice carrying the *iFlp*$^{MTomato\text{-}Cre/MYFP}$ allele combined with either the published
964 *R26*$^{CAG\text{-}FlpoERT2}$ or the newly generated *Tg(Ins-CAG-FlpoERT2)*^{F2} allele. **e,** Chart showing the lack of

965 leakiness of the *Tg(Ins-CAG-FlpoERT2)*^{F2} allele. In the absence of tamoxifen the *iFlp*$^{MTomato\text{-}Cre/MYFP}$
966 allele is not recombined.
967

968 **Supplementary Figure 4: Ratiometric iFlpMosaics show that *Myc*^{KO} cells have a stronger**
969 **competitive disadvantage in blood than ECs. a,b,** Representative FACS plots showing that in both
970 the heart and the lung CD45+ blood cells are much more affected by *Myc* deletion than CD31+
971 endothelial cells.

972

973 **Supplementary Figure 5: Mapping the clonal expansion of single mutant and wildtype cells with**
974 ***iFlpMosaics*. a,b,** Representative confocal images (large tile scans), at low magnification, of entire P20
975 liver sections of mice carrying the indicated alleles. Recombination of the reporter alleles was induced
976 at P1 and resulted in different recombination frequencies. Right panels show automatic image
977 processing results using Fiji scripts, that generate spatial maps of dual-labelled clones of cells (with
978 membrane and nuclear labelling). The bigger the circle, the bigger the clone. **c,** Quantification and
979 representative confocal micrographs of proliferative pancreatic cells (Ki67+ in cycle or EdU+ in s-
980 phase) at different postnatal stages. **d,** Quantification and representative confocal micrograph of
981 Ki67+/DAPI+ cells in the adult liver. **e,** Representative confocal micrographs of adult liver sections
982 from control and *Myc floxed* mice combined with the indicated alleles. Left panels show endogenous
983 fluorescent signals from the reporter alleles and left panels show sections from the same mice
984 immunostained with antibodies that bind to DsRed (detects MTomato and H2B-Cherry), or GFP
985 (detects MYFP and H2B-GFP) or the HA epitope (detects MbTFP1 and H2B-Cerulean). Right panels
986 show automatic image processing results using Fiji scripts, that generate spatial maps of dual-labelled
987 clones of cells (with membrane and nuclear labelling) reveal hepatocytes ploidy and clone size. Chart
988 showing that in control mice, MYFP+ (WT) and MTomato+ (WT) diploid cells occur in similar
989 proportions, while in *Myc* floxed mutants, MTomato+ (*Myc*^{KO}) diploid cells are more frequently
990 binucleated and give rise to less 2-cell mononucleated clones than MYFP+ (*Myc*^{WT}) cells.

991

992 **Supplementary Figure 6: *iFlp/Dre*^{Progenitor} enables the induction of genetic mosaics from a single**
993 **progenitor cell. a,** Representative confocal micrograph of a P7 retina of an animals carrying the
994 indicated alleles and induced with 4-OHT at P3. After induction of the ***iFlp/Dre*^{Progenitor}** allele, cells will
995 express the nuclei marker H2B-V5 and FlpO. FlpO will after some time and cell division recombine
996 the *iFlp*$^{MTomato\text{-}Cre/MYFP}$ allele generating MbYFP+ and MbTomato+ progeny cells derived from a single
997 initial recombination event.

998

Supplementary Figure 7: Single cell RNA-seq analysis combined with ratiometric *iFlp*^{Mosaics} uncovers cell-autonomous gene function in diverse cell types. a, UMAP and barplot showing the identified clusters and their frequencies among YFP+ (*Rbpj*^{WT}) and Tomato+ (*Rbpj*^{KO}) smooth muscle cells. Dot plot showing the frequency (size) and expression level (intensity of color) for the top cluster marker genes. **b,** Top differentially expressed genes per cluster between YFP+ (*Rbpj*^{WT}) and Tomato+ (*Rbpj*^{KO}) smooth muscle cells. The proliferative cluster becomes more proliferative (MKi67+) and less arrested (Cdkn1a) in the absence of Rbpj/Hes1. **c,** GSEA hallmark analysis for the SMC cluster reveals only one significantly deregulated pathway. **d**, Cell types or clusters in which *Rbpj* mosaic deletion with ***iFlp***^{Mosaics} did not affect their overall relative ratios (see Figure 7), also do not significantly change their subclusters spatial mapping (UMAPs) or transcriptome (Dot plots) or GSEA pathways.

1034 **References**

1035

1036 Aran, D., Looney, A.P., Liu, L., Wu, E., Fong, V., Hsu, A., Chak, S., Naikawadi, R.P., Wolters, P.J.,
1037 Abate, A.R., et al. (2019). Reference-based analysis of lung single-cell sequencing reveals a
1038 transitional profibrotic macrophage. Nat Immunol *20*, 163-172. 10.1038/s41590-018-0276-y.
1039 Cai, D., Cohen, K.B., Luo, T., Lichtman, J.W., and Sanes, J.R. (2013). Improved tools for the
1040 Brainbow toolbox. Nature methods *10*, 540-547.
1041 Claveria, C., Giovinazzo, G., Sierra, R., and Torres, M. (2013). Myc-driven endogenous cell
1042 competition in the early mammalian embryo. Nature *500*, 39-44. 10.1038/nature12389.
1043 Contreras, X., Amberg, N., Davaatseren, A., Hansen, A.H., Sonntag, J., Andersen, L., Bernthaler, T.,
1044 Streicher, C., Heger, A., Johnson, R.L., et al. (2021). A genome-wide library of MADM mice
1045 for single-cell genetic mosaic analysis. Cell reports *35*, 109274.
1046 10.1016/j.celrep.2021.109274.
1047 de Alboran, I.M., O'Hagan, R.C., Gartner, F., Malynn, B., Davidson, L., Rickert, R., Rajewsky, K.,
1048 DePinho, R.A., and Alt, F.W. (2001). Analysis of C-MYC function in normal cells via
1049 conditional gene-targeted mutation. Immunity *14*, 45-55.
1050 Dharaneeswaran, H., Abid, M.R., Yuan, L., Dupuis, D., Beeler, D., Spokes, K.C., Janes, L., Sciuto,
1051 T., Kang, P.M., Jaminet, S.S., et al. (2014). FOXO1-mediated activation of Akt plays a
1052 critical role in vascular homeostasis. Circ Res *115*, 238-251.
1053 10.1161/CIRCRESAHA.115.303227.
1054 Eijkelenboom, A., and Burgering, B.M. (2013). FOXOs: signalling integrators for homeostasis
1055 maintenance. Nat Rev Mol Cell Biol *14*, 83-97. 10.1038/nrm3507.
1056 Ema, M., Takahashi, S., and Rossant, J. (2006). Deletion of the selection cassette, but not cis-acting
1057 elements, in targeted Flk1-lacZ allele reveals Flk1 expression in multipotent mesodermal
1058 progenitors. Blood *107*, 111-117. 10.1182/blood-2005-05-1970.
1059 Fernandez-Chacon, M., Casquero-Garcia, V., Luo, W., Francesca Lunella, F., Ferreira Rocha, S., Del
1060 Olmo-Cabrera, S., and Benedito, R. (2019). iSuRe-Cre is a genetic tool to reliably induce and
1061 report Cre-dependent genetic modifications. Nature communications *10*, 2262.
1062 10.1038/s41467-019-10239-4.
1063 Han, H., Tanigaki, K., Yamamoto, N., Kuroda, K., Yoshimoto, M., Nakahata, T., Ikuta, K., and
1064 Honjo, T. (2002). Inducible gene knockout of transcription factor recombination signal
1065 binding protein-J reveals its essential role in T versus B lineage decision. Int Immunol *14*,
1066 637-645.
1067 Hansen, A.H., and Hippenmeyer, S. (2020). Non-Cell-Autonomous Mechanisms in Radial Projection
1068 Neuron Migration in the Developing Cerebral Cortex. Front Cell Dev Biol *8*, 574382.
1069 10.3389/fcell.2020.574382.
1070 Hansen, A.H., Pauler, F.M., Riedl, M., Streicher, C., Heger, A., Laukoter, S., Sommer, C., Nicolas,
1071 A., Hof, B., Tsai, L.H., et al. (2022). Tissue-Wide Effects Override Cell-Intrinsic Gene
1072 Function in Radial Neuron Migration. Oxford Open Neuroscience *1*. 10.1093/oons/kvac009.
1073 Hao, Y., Hao, S., Andersen-Nissen, E., Mauck, W.M., 3rd, Zheng, S., Butler, A., Lee, M.J., Wilk,
1074 A.J., Darby, C., Zager, M., et al. (2021). Integrated analysis of multimodal single-cell data.
1075 Cell *184*, 3573-3587 e3529. 10.1016/j.cell.2021.04.048.
1076 He, C., Hu, H., Braren, R., Fong, S.-Y., Trumpp, A., Carlson, T.R., and Wang, R.A. (2008). c-myc in
1077 the hematopoietic lineage is crucial for its angiogenic function in the mouse embryo.
1078 Development *135*, 2467-2477. 10.1242/dev.020131.
1079 He, L., Pu, W., Liu, X., Zhang, Z., Han, M., Li, Y., Huang, X., Han, X., Li, Y., Liu, K., et al. (2021).
1080 Proliferation tracing reveals regional hepatocyte generation in liver homeostasis and repair.
1081 Science *371*, eabc4346. doi:10.1126/science.abc4346.
1082 Hunter, N.L., Awatramani, R.B., Farley, F.W., and Dymecki, S.M. (2005). Ligand-activated Flpe for
1083 temporally regulated gene modifications. Genesis *41*, 99-109. 10.1002/gene.20101.
1084 Knoepfler, P.S., Cheng, P.F., and Eisenman, R.N. (2002). N-myc is essential during neurogenesis for
1085 the rapid expansion of progenitor cell populations and the inhibition of neuronal
1086 differentiation. Genes Dev *16*, 2699-2712. 10.1101/gad.1021202.

1087 Kranz, A., Fu, J., Duerschke, K., Weidlich, S., Naumann, R., Stewart, A.F., and Anastassiadis, K.
1088 (2010). An improved Flp deleter mouse in C57Bl/6 based on Flpo recombinase. Genesis *48*,
1089 512-520. 10.1002/dvg.20641.
1090 Lao, Z., Raju, G.P., Bai, C.B., and Joyner, A.L. (2012). MASTR: a technique for mosaic mutant
1091 analysis with spatial and temporal control of recombination using conditional floxed alleles in
1092 mice. Cell reports *2*, 386-396. 10.1016/j.celrep.2012.07.004.
1093 Liu, J., Willet, S.G., Bankaitis, E.D., Xu, Y., Wright, C.V., and Gu, G. (2013). Non-parallel
1094 recombination limits cre-loxP-based reporters as precise indicators of conditional genetic
1095 manipulation. Genesis *51*, 436-442. 10.1002/dvg.22384.
1096 Livet, J., Weissman, T.A., Kang, H., Draft, R.W., Lu, J., Bennis, R.A., Sanes, J.R., and Lichtman,
1097 J.W. (2007). Transgenic strategies for combinatorial expression of fluorescent proteins in the
1098 nervous system. Nature *450*, 56-62. nature06293 [pii]

1099 10.1038/nature06293.
1100 Loonstra, A., Vooijs, M., Beverloo, H.B., Allak, B.A., van Drunen, E., Kanaar, R., Berns, A., and
1101 Jonkers, J. (2001). Growth inhibition and DNA damage induced by Cre recombinase in
1102 mammalian cells. Proc Natl Acad Sci U S A *98*, 9209-9214. 10.1073/pnas.161269798.
1103 Luo, W., Garcia-Gonzalez, I., Fernández-Chacón, M., Casquero-Garcia, V., Sanchez-Muñoz, M.S.,
1104 Mühleder, S., Garcia-Ortega, L., Andrade, J., Potente, M., and Benedito, R. (2021).
1105 Arterialization requires the timely suppression of cell growth. Nature *589*, 437-441.
1106 10.1038/s41586-020-3018-x.
1107 Madisen, L., Zwingman, T.A., Sunkin, S.M., Oh, S.W., Zariwala, H.A., Gu, H., Ng, L.L., Palmiter,
1108 R.D., Hawrylycz, M.J., Jones, A.R., et al. (2010). A robust and high-throughput Cre reporting
1109 and characterization system for the whole mouse brain. Nat Neurosci *13*, 133-140.
1110 10.1038/nn.2467.
1111 Munoz-Martin, N., Sierra, R., Schimmang, T., Villa Del Campo, C., and Torres, M. (2019). Myc is
1112 dispensable for cardiomyocyte development but rescues Mycn-deficient hearts through
1113 functional replacement and cell competition. Development *146*. 10.1242/dev.170753.
1114 Naiche, L.A., and Papaioannou, V.E. (2007). Cre activity causes widespread apoptosis and lethal
1115 anemia during embryonic development. Genesis *45*, 768-775. 10.1002/dvg.20353.
1116 Paik, J.H., Kollipara, R., Chu, G., Ji, H., Xiao, Y., Ding, Z., Miao, L., Tothova, Z., Horner, J.W.,
1117 Carrasco, D.R., et al. (2007). FoxOs are lineage-restricted redundant tumor suppressors and
1118 regulate endothelial cell homeostasis. Cell *128*, 309-323. 10.1016/j.cell.2006.12.029.
1119 Pontes-Quero, S., Fernández-Chacón, M., Luo, W., Lunella, F.F., Casquero-Garcia, V., Garcia-
1120 Gonzalez, I., Hermoso, A., Rocha, S.F., Bansal, M., and Benedito, R. (2019). High mitogenic
1121 stimulation arrests angiogenesis. Nature communications *10*, 2016. 10.1038/s41467-019-
1122 09875-7.
1123 Pontes-Quero, S., Heredia, L., Casquero-Garcia, V., Fernandez-Chacon, M., Luo, W., Hermoso, A.,
1124 Bansal, M., Garcia-Gonzalez, I., Sanchez-Munoz, M.S., Perea, J.R., et al. (2017). Dual
1125 ifgMosaic: A Versatile Method for Multispectral and Combinatorial Mosaic Gene-Function
1126 Analysis. Cell *170*, 800-814 e818. 10.1016/j.cell.2017.07.031.
1127 Radtke, F., Wilson, A., Stark, G., Bauer, M., van Meerwijk, J., MacDonald, H.R., and Aguet, M.
1128 (1999). Deficient T Cell Fate Specification in Mice with an Induced Inactivation of Notch1.
1129 Immunity *10*, 547-558. 10.1016/s1074-7613(00)80054-0.
1130 Rashbrook, V.S., Brash, J.T., and Ruhrberg, C. (2022). Cre toxicity in mouse models of
1131 cardiovascular physiology and disease. Nature Cardiovascular Research *1*, 806-816.
1132 10.1038/s44161-022-00125-6.
1133 Rodriguez, C.I., Buchholz, F., Galloway, J., Sequerra, R., Kasper, J., Ayala, R., Stewart, A.F., and
1134 Dymecki, S.M. (2000). High-efficiency deleter mice show that FLPe is an alternative to Cre-
1135 loxP. Nat Genet *25*, 139-140.
1136 Schmidt-Supprian, M., and Rajewsky, K. (2007). Vagaries of conditional gene targeting. Nat
1137 Immunol *8*, 665-668. 10.1038/ni0707-665.
1138 Sharma, P., Yan, F., Doronina, V.A., Escuin-Ordinas, H., Ryan, M.D., and Brown, J.D. (2012). 2A
1139 peptides provide distinct solutions to driving stop-carry on translational recoding. Nucleic
1140 Acids Res *40*, 3143-3151. 10.1093/nar/gkr1176.

1141 Siebel, C., and Lendahl, U. (2017). Notch Signaling in Development, Tissue Homeostasis, and
1142 Disease. Physiol Rev *97*, 1235-1294. 10.1152/physrev.00005.2017.
1143 Snippert, H.J., van der Flier, L.G., Sato, T., van Es, J.H., van den Born, M., Kroon-Veenboer, C.,
1144 Barker, N., Klein, A.M., van Rheenen, J., Simons, B.D., and Clevers, H. (2010). Intestinal
1145 crypt homeostasis results from neutral competition between symmetrically dividing Lgr5
1146 stem cells. Cell *143*, 134-144. 10.1016/j.cell.2010.09.016.
1147 Srinivas, S., Watanabe, T., Lin, C.S., William, C.M., Tanabe, Y., Jessell, T.M., and Costantini, F.
1148 (2001). Cre reporter strains produced by targeted insertion of EYFP and ECFP into the
1149 ROSA26 locus. BMC Dev Biol *1*, 4.
1150 Wang, Y., Nakayama, M., Pitulescu, M.E., Schmidt, T.S., Bochenek, M.L., Sakakibara, A., Adams,
1151 S., Davy, A., Deutsch, U., Luthi, U., et al. (2010). Ephrin-B2 controls VEGF-induced
1152 angiogenesis and lymphangiogenesis. Nature *465*, 483-486. nature09002 [pii]

1153 10.1038/nature09002.
1154 Wilhelm, K., Happel, K., Eelen, G., Schoors, S., Oellerich, M.F., Lim, R., Zimmermann, B., Aspalter,
1155 I.M., Franco, C.A., Boettger, T., et al. (2016). FOXO1 couples metabolic activity and growth
1156 state in the vascular endothelium. Nature *529*, 216-220. 10.1038/nature16498.
1157 Zong, H. (2014). Generation and applications of MADM-based mouse genetic mosaic system.
1158 Methods Mol Biol *1194*, 187-201. 10.1007/978-1-4939-1215-5_10.
1159 Zong, H., Espinosa, J.S., Su, H.H., Muzumdar, M.D., and Luo, L. (2005). Mosaic analysis with
1160 double markers in mice. Cell *121*, 479-492. 10.1016/j.cell.2005.02.012.

1161

1162

1163

1164

Figure 1

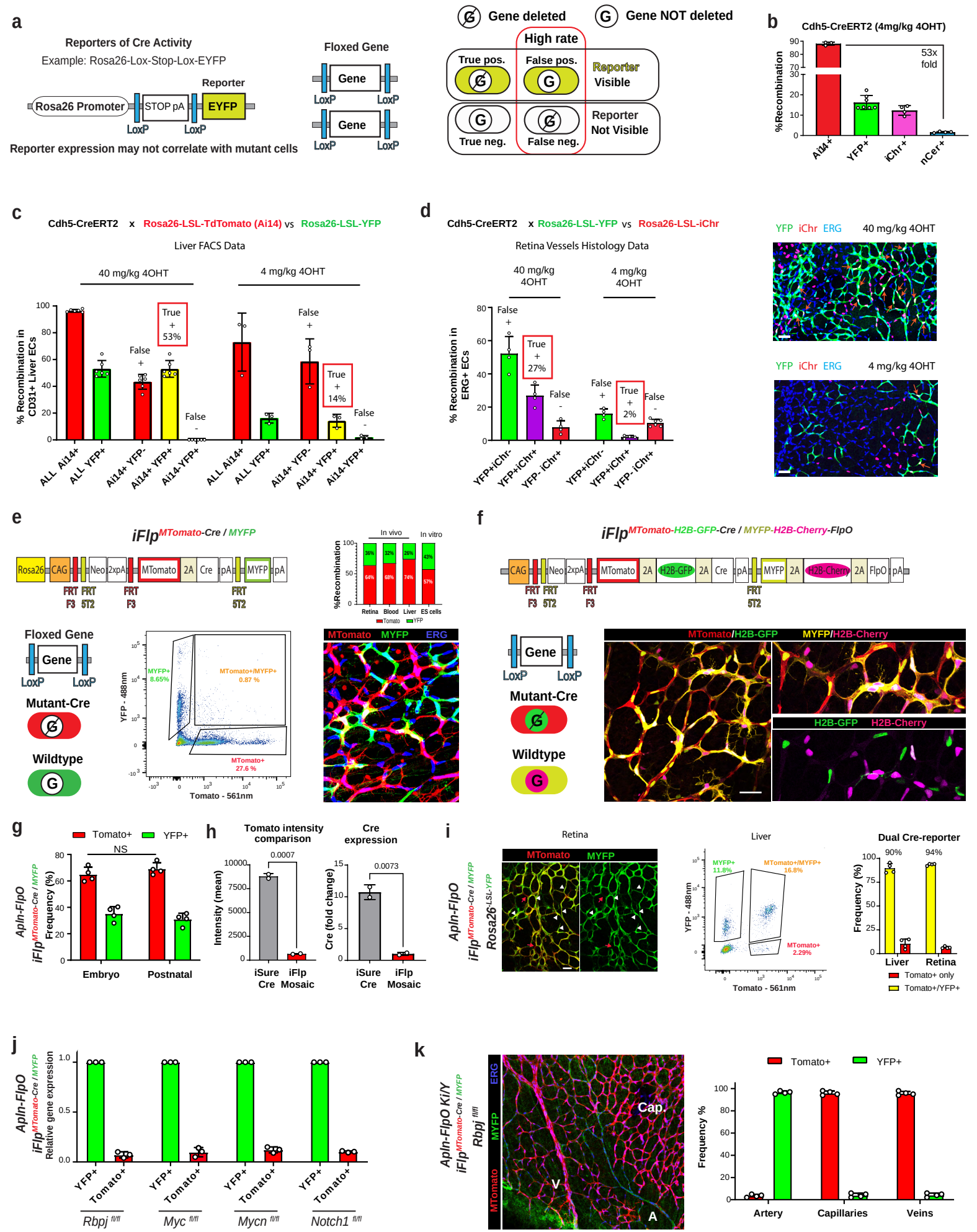
a
Reporters of Cre Activity
Example: Rosa26-Lox-Stop-Lox-EYFP
Reporter
Rosa26 Promoter
STOP pA
EYFP
LoxP
LoxP
Reporter expression may not correlate with mutant cells
Floxed Gene
Gene
Gene deleted
Gene NOT deleted
High rate
True pos.
False pos.
Reporter Visible
True neg.
False neg.
Reporter Not Visible
b
Cdh5-CreERT2 (4mg/kg 4OHT)
%Recombination
53x fold
Ai14+
YFP+
iChr+
nCer+
c
Cdh5-CreERT2 x Rosa26-LSL-TdTomato (Ai14) vs Rosa26-LSL-YFP
Liver FACS Data
40 mg/kg 4OHT
4 mg/kg 4OHT
% Recombination in CD31+ Liver ECs
True + 53%
False +
False -
True + 14%
ALL Ai14+
ALL YFP+
Ai14+ YFP-
Ai14+ YFP+
Ai14-YFP+
d
Cdh5-CreERT2 x Rosa26-LSL-YFP vs Rosa26-LSL-iChr
Retina Vessels Histology Data
40 mg/kg 4OHT
4 mg/kg 4OHT
% Recombination in ERG+ ECs
True + 27%
True + 2%
YFP+iChr-
YFP+iChr+
YFP- iChr+
YFP iChr ERG
40 mg/kg 4OHT
4 mg/kg 4OHT
e
iFlp MTomato-Cre / MYFP
Rosa26
CAG
Neo
2xpA
MTomato
2A
Cre
pA
MYFP
FRT F3
FRT 5T2
In vivo
In vitro
%Recombination
Retina
Blood
Liver
ES cells
Tomato
YFP
Floxed Gene
Gene
LoxP
Mutant-Cre
Wildtype
MYFP+ 8.65%
MTomato+/MYFP+ 0.87 %
MTomato+ 27.6 %
YFP - 488nm
Tomato - 561nm
MTomato MYFP ERG
f
iFlp MTomato-H2B-GFP-Cre / MYFP-H2B-Cherry-FlpO
H2B-GFP
H2B-Cherry
FlpO
Gene
Mutant-Cre
Wildtype
MTomato/H2B-GFP
MYFP/H2B-Cherry
H2B-GFP H2B-Cherry
g
Tomato+
YFP+
NS
Apln-FlpO
iFlp MTomato-Cre / MYFP
Frequency (%)
Embryo
Postnatal
h
Tomato intensity comparison
Cre expression
0.0007
0.0073
Intensity (mean)
Cre (fold change)
iSure Cre
iFlp Mosaic
i
Retina
Liver
Dual Cre-reporter
Apln-FlpO
iFlp MTomato-Cre / MYFP
Rosa26 LSL-YFP
MTomato
MYFP
MYFP+ 11.8%
MTomato+/MYFP+ 16.8%
MTomato+ 2.29%
YFP - 488nm
Tomato - 561nm
90%
94%
Frequency (%)
Liver
Retina
Tomato+ only
Tomato+/YFP+
j
Apln-FlpO
iFlp MTomato-Cre / MYFP
Relative gene expression
YFP+
Tomato+
Rbpj fl/fl
Myc fl/fl
Mycn fl/fl
Notch1 fl/fl
k
Apln-FlpO Ki/Y
iFlp MTomato-Cre / MYFP
Rbpj fl/fl
ERG
MYFP
MTomato
Cap
V
A
Tomato+
YFP+
Frequency %
Artery
Capillaries
Veins

Figure 2

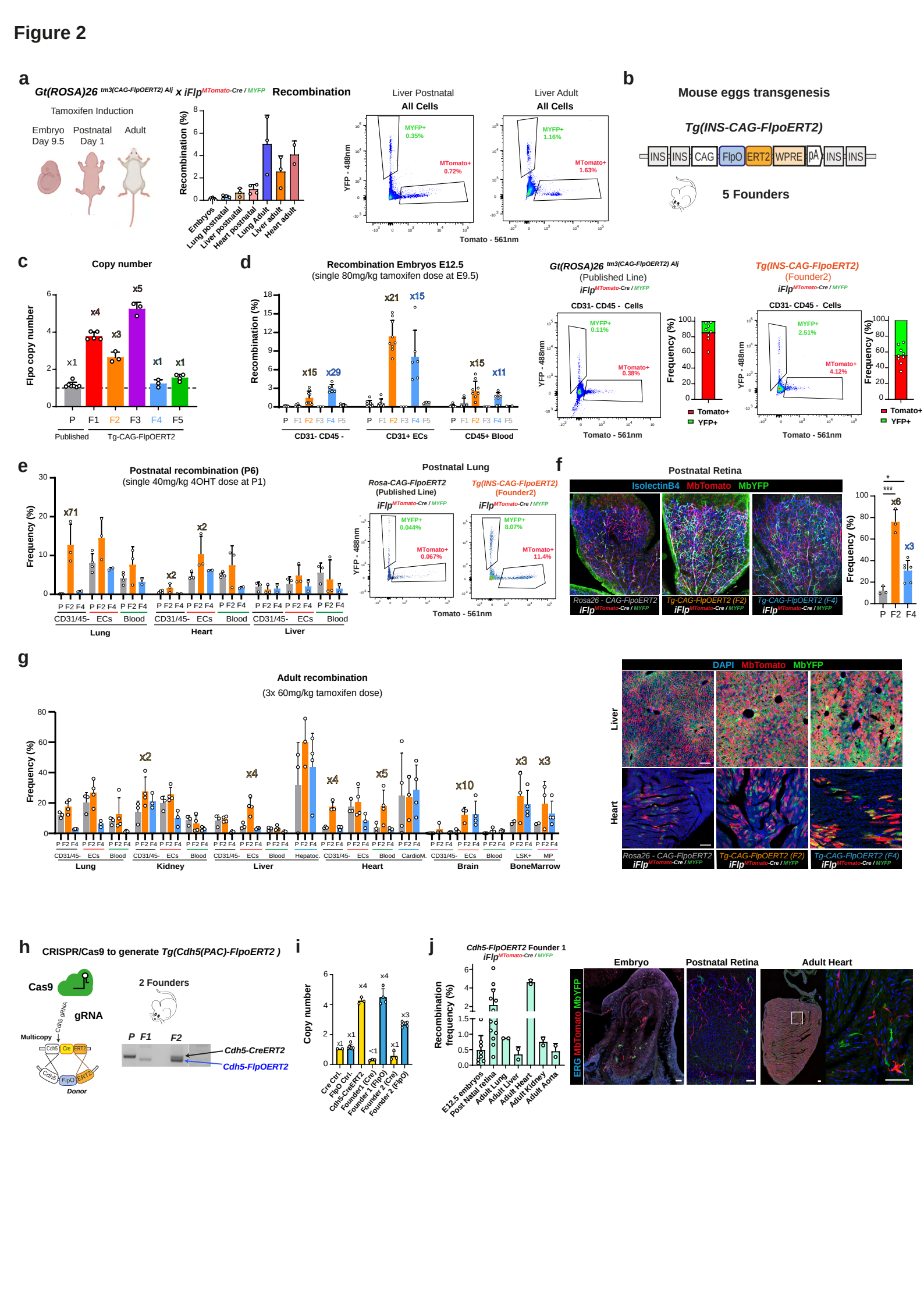
a
Gt(ROSA)26 tm3(CAG-FlpOERT2) Alj x iFlpMTomato-Cre / MYFP
Recombination
Tamoxifen Induction
Embryo Day 9.5
Postnatal Day 1
Adult
Recombination (%)
Embryos
Lung postnatal
Liver postnatal
Heart postnatal
Lung Adult
Liver adult
Heart adult
Liver Postnatal
All Cells
MYFP+ 0.35%
MTomato+ 0.72%
Liver Adult
All Cells
MYFP+ 1.16%
MTomato+ 1.63%
YFP - 488nm
Tomato - 561nm
b
Mouse eggs transgenesis
Tg(INS-CAG-FlpoERT2)
INS INS CAG FlpO ERT2 WPRE bA INS INS
5 Founders
c
Copy number
Flpo copy number
x1 x4 x3 x5 x1 x1
P F1 F2 F3 F4 F5
Published
Tg-CAG-FlpOERT2
d
Recombination Embryos E12.5
(single 80mg/kg tamoxifen dose at E9.5)
Recombination (%)
x15 x29 x21 x15 x15 x11
CD31- CD45 -
CD31+ ECs
CD45+ Blood
Gt(ROSA)26 tm3(CAG-FlpOERT2) Alj
(Published Line)
iFlpMTomato-Cre / MYFP
CD31- CD45 - Cells
MYFP+ 0.11%
MTomato+ 0.38%
Frequency (%)
Tomato+
YFP+
Tg(INS-CAG-FlpoERT2)
(Founder2)
iFlpMTomato-Cre / MYFP
CD31- CD45 - Cells
MYFP+ 2.51%
MTomato+ 4.12%
Tomato+
YFP+
e
Postnatal recombination (P6)
(single 40mg/kg 4OHT dose at P1)
Frequency (%)
x71 x2 x2
CD31/45- ECs Blood
Lung
Heart
Liver
Postnatal Lung
Rosa-CAG-FlpoERT2
(Published Line)
iFlpMTomato-Cre / MYFP
MYFP+ 0.044%
MTomato+ 0.067%
Tg(INS-CAG-FlpoERT2)
(Founder2)
iFlpMTomato-Cre / MYFP
MYFP+ 8.07%
MTomato+ 11.4%
f
Postnatal Retina
IsolectinB4 MbTomato MbYFP
Rosa26 - CAG-FlpoERT2
Tg-CAG-FlpOERT2 (F2)
Tg-CAG-FlpOERT2 (F4)
iFlpMTomato-Cre / MYFP
Frequency (%)
x6 x3
P F2 F4
g
Adult recombination
(3x 60mg/kg tamoxifen dose)
Frequency (%)
x2 x4 x4 x5 x10 x3 x3
CD31/45- ECs Blood
Lung
Kidney
Liver
Hepatoc.
Heart
CardioM.
Brain
LSK+ MP
BoneMarrow
DAPI MbTomato MbYFP
Liver
Heart
Rosa26 - CAG-FlpoERT2
Tg-CAG-FlpOERT2 (F2)
Tg-CAG-FlpOERT2 (F4)
iFlpMTomato-Cre / MYFP
h
CRISPR/Cas9 to generate Tg(Cdh5(PAC)-FlpoERT2)
Cas9
gRNA
Cdh5 gRNA
Multicopy
Cdh5 Cre ERT2
Cdh5 FlpO ERT2
Donor
2 Founders
P F1 F2
Cdh5-CreERT2
Cdh5-FlpOERT2
i
Copy number
x1 x1 x4 <1 x4 x1 x3
Cre Ctrl.
FlpO Ctrl.
Cdh5-CreERT2
Founder1 (Cre)
Founder1 (FlpO)
Founder 2 (Cre)
Founder 2 (FlpO)
j
Cdh5-FlpOERT2 Founder 1
iFlpMTomato-Cre / MYFP
Recombination frequency (%)
E12.5 embryos
Post Natal retina
Adult Lung
Adult Liver
Adult Heart
Adult Kidney
Adult Aorta
Embryo
Postnatal Retina
Adult Heart
ERG MbTomato MbYFP

Figure 3

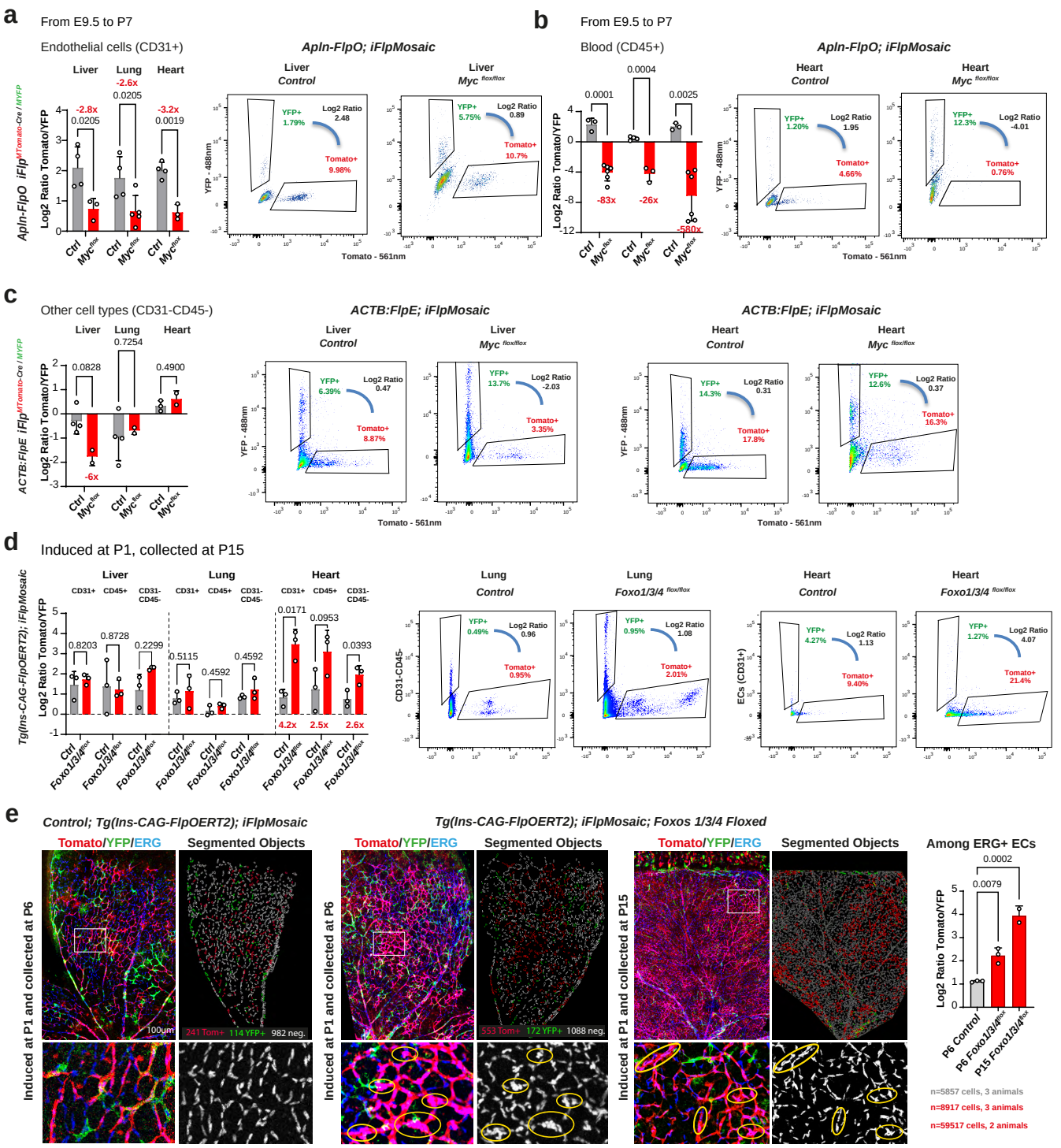
a
From E9.5 to P7
Endothelial cells (CD31+)
Apln-FlpO; iFlpMosaic
Liver
Lung
Heart
Log2 Ratio Tomato/YFP
-2.8x
0.0205
-2.6x
0.0205
-3.2x
0.0019
Ctrl
Myc flox
Liver Control
Liver Myc flox/flox
YFP+ 1.79%
Log2 Ratio 2.48
Tomato+ 9.98%
YFP+ 5.75%
Log2 Ratio 0.89
Tomato+ 10.7%
YFP - 488nm
Tomato - 561nm
b
From E9.5 to P7
Blood (CD45+)
Apln-FlpO; iFlpMosaic
0.0001
0.0004
0.0025
-83x
-26x
-580x
Heart Control
Heart Myc flox/flox
YFP+ 1.20%
Log2 Ratio 1.95
Tomato+ 4.66%
YFP+ 12.3%
Log2 Ratio -4.01
Tomato+ 0.76%
c
Other cell types (CD31-CD45-)
ACTB:FlpE; iFlpMosaic
0.0828
0.7254
0.4900
-6x
Liver Control
Liver Myc flox/flox
YFP+ 6.39%
Log2 Ratio 0.47
Tomato+ 8.87%
YFP+ 13.7%
Log2 Ratio -2.03
Tomato+ 3.35%
Heart Control
Heart Myc flox/flox
YFP+ 14.3%
Log2 Ratio 0.31
Tomato+ 17.8%
YFP+ 12.6%
Log2 Ratio 0.37
Tomato+ 16.3%
d
Induced at P1, collected at P15
Tg(Ins-CAG-FlpOERT2); iFlpMosaic
CD31+
CD45+
CD31-CD45-
0.8203
0.8728
0.2299
0.5115
0.4592
0.4592
0.0171
0.0953
0.0393
4.2x
2.5x
2.6x
Lung Control
Lung Foxo1/3/4 flox/flox
Heart Control
Heart Foxo1/3/4 flox/flox
CD31-CD45-
ECs (CD31+)
YFP+ 0.49%
Log2 Ratio 0.96
Tomato+ 0.95%
YFP+ 0.95%
Log2 Ratio 1.08
Tomato+ 2.01%
YFP+ 4.27%
Log2 Ratio 1.13
Tomato+ 9.40%
YFP+ 1.27%
Log2 Ratio 4.07
Tomato+ 21.4%
e
Control; Tg(Ins-CAG-FlpOERT2); iFlpMosaic
Tg(Ins-CAG-FlpOERT2); iFlpMosaic; Foxos 1/3/4 Floxed
Tomato/YFP/ERG
Segmented Objects
Induced at P1 and collected at P6
Induced at P1 and collected at P15
100µm
241 Tom+ 114 YFP+ 982 neg.
553 Tom+ 172 YFP+ 1088 neg.
Among ERG+ ECs
0.0002
0.0079
P6 Control
P6 Foxo1/3/4 flox
P15 Foxo1/3/4 flox
n=5857 cells, 3 animals
n=8917 cells, 3 animals
n=59517 cells, 2 animals

Figure 4

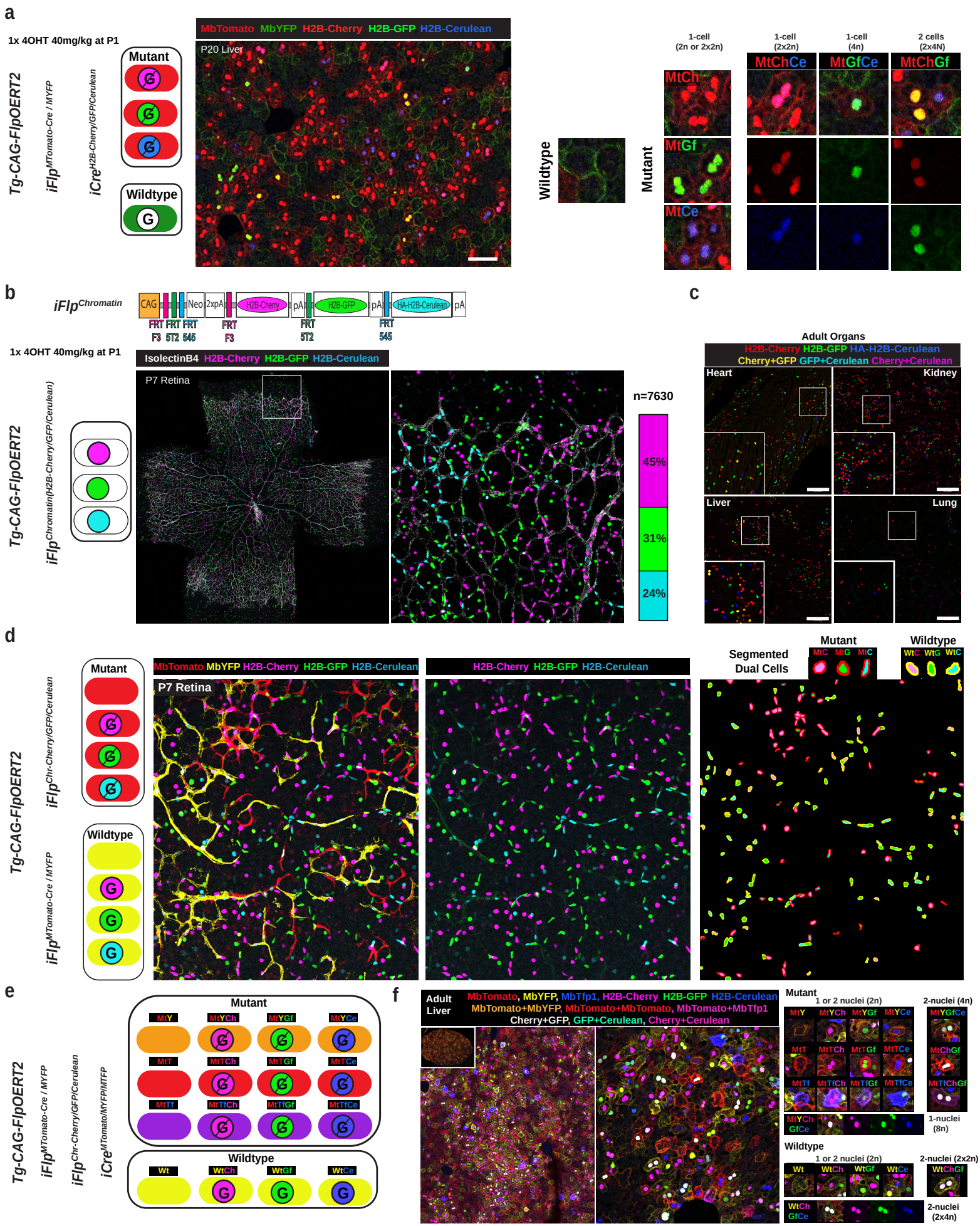
a
1x 4OHT 40mg/kg at P1
Tg-CAG-FlpOERT2
iFlpMTomato-Cre / MYFP
iCreH2B-Cherry/GFP/Cerulean
Mutant
Wildtype
MbTomato MbYFP H2B-Cherry H2B-GFP H2B-Cerulean
P20 Liver
Wildtype
Mutant
1-cell (2n or 2x2n)
1-cell (2x2n)
1-cell (4n)
2 cells (2x4N)
MtCh
MtGf
MtCe
MtChCe
MtGfCe
MtChGf
b
iFlpChromatin
CAG
Neo
2xpA
H2B-Cherry
pA
H2B-GFP
HA-H2B-Cerulean
FRT F3
FRT 5T2
FRT 545
1x 4OHT 40mg/kg at P1
IsolectinB4 H2B-Cherry H2B-GFP H2B-Cerulean
P7 Retina
n=7630
45%
31%
24%
c
Adult Organs
H2B-Cherry H2B-GFP HA-H2B-Cerulean
Cherry+GFP GFP+Cerulean Cherry+Cerulean
Heart
Kidney
Liver
Lung
d
Tg-CAG-FlpOERT2
iFlpChr-Cherry/GFP/Cerulean
iFlpMTomato-Cre / MYFP
Mutant
Wildtype
MbTomato MbYFP H2B-Cherry H2B-GFP H2B-Cerulean
P7 Retina
H2B-Cherry H2B-GFP H2B-Cerulean
Segmented Dual Cells
Mutant
Wildtype
MtC MtG MtC
WtC WtG WtC
e
Tg-CAG-FlpOERT2
iFlpMTomato-Cre / MYFP
iFlpChr-Cherry/GFP/Cerulean
iCreMTomato/MYFP/MTFP
Mutant
MtY MtYCh MtYGf MtYCe
MtT MtTCh MtTGf MtTCe
MtTf MtTfCh MtTfGf MtTfCe
Wildtype
Wt WtCh WtGf WtCe
f
Adult Liver
MbTomato, MbYFP, MbTfp1, H2B-Cherry H2B-GFP H2B-Cerulean
MbTomato+MbYFP, MbTomato+MbTomato, MbTomato+MbTfp1
Cherry+GFP, GFP+Cerulean, Cherry+Cerulean
Mutant
1 or 2 nuclei (2n)
2-nuclei (4n)
MtY MtYCh MtYGf MtYCe
MtT MtTCh MtTGf MtTCe
MtTf MtTfCh MtTfGf MtTfCe
MtYGfCe
MtChGf
MtTfChGf
MtYCh GfCe
1-nuclei (8n)
Wildtype
1 or 2 nuclei (2n)
2-nuclei (2x2n)
Wt WtCh WtGf WtCe
WtChGf
WtCh GfCe
2-nuclei (2x4n)

Figure 5

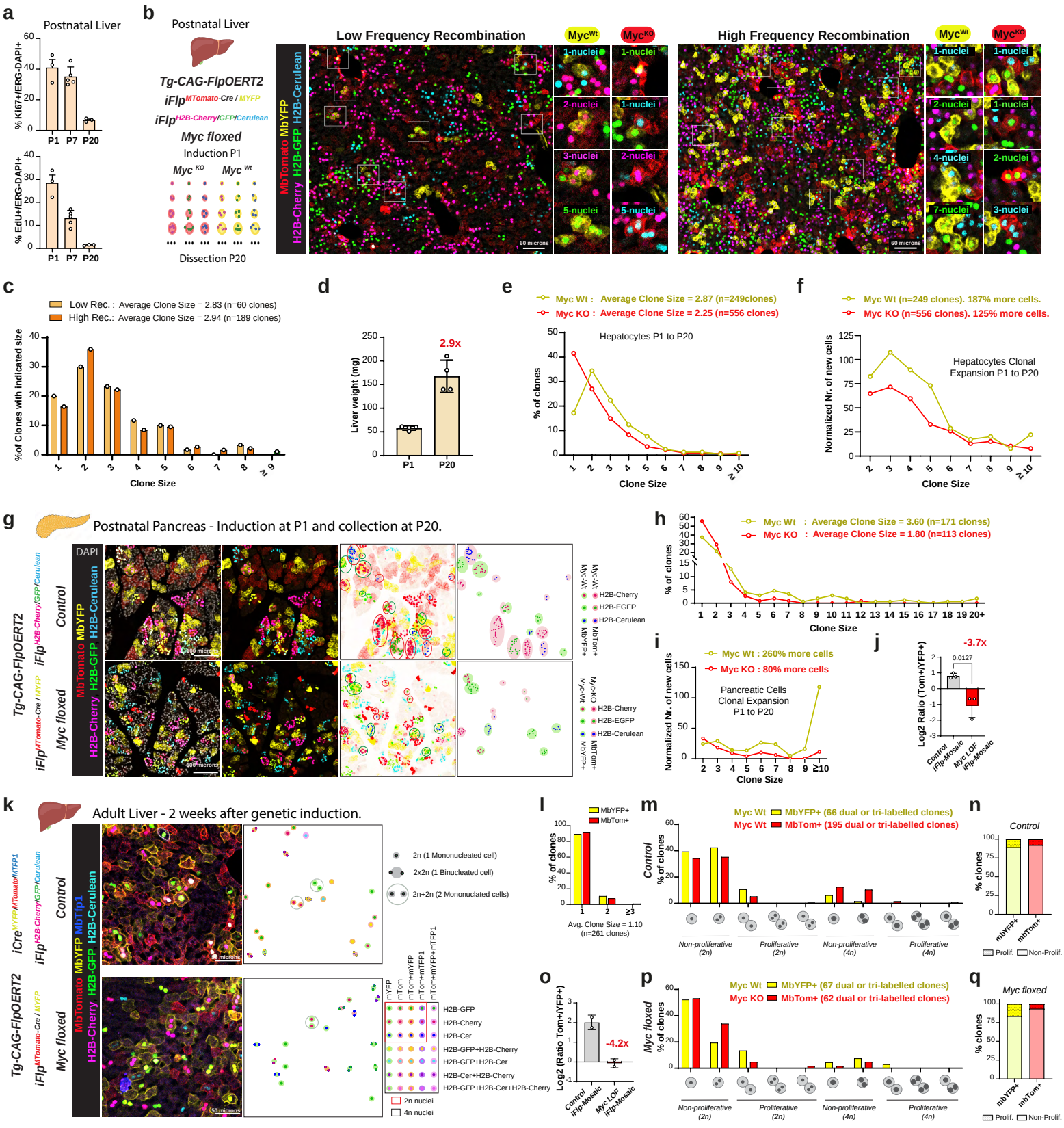
a
Postnatal Liver
% Ki67+/ERG-DAPI+
% EdU+/ERG-DAPI+
P1 P7 P20
b
Postnatal Liver
Tg-CAG-FlpOERT2
iFlp MTomato-Cre / MYFP
iFlp H2B-Cherry/GFP/Cerulean
Myc floxed
Induction P1
Myc KO
Myc Wt
Dissection P20
Low Frequency Recombination
High Frequency Recombination
MbTomato MbYFP
H2B-Cherry H2B-GFP H2B-Cerulean
1-nuclei
2-nuclei
3-nuclei
4-nuclei
5-nuclei
7-nuclei
60 microns
c
Low Rec. : Average Clone Size = 2.83 (n=60 clones)
High Rec.: Average Clone Size = 2.94 (n=189 clones)
%of Clones with indicated size
Clone Size
d
2.9x
Liver weight (mg)
P1
P20
e
Myc Wt : Average Clone Size = 2.87 (n=249clones)
Myc KO : Average Clone Size = 2.25 (n=556 clones)
Hepatocytes P1 to P20
% of clones
Clone Size
f
Myc Wt (n=249 clones). 187% more cells.
Myc KO (n=556 clones). 125% more cells.
Hepatocytes Clonal Expansion P1 to P20
Normalized Nr. of new cells
Clone Size
g
Postnatal Pancreas - Induction at P1 and collection at P20.
Tg-CAG-FlpOERT2
iFlp MTomato-Cre / MYFP
iFlp H2B-Cherry/GFP/Cerulean
Control
Myc floxed
DAPI
MbTomato MbYFP
H2B-Cherry H2B-GFP H2B-Cerulean
400 microns
Myc-Wt
Myc-KO
MbYFP+
MbTom+
H2B-Cherry
H2B-EGFP
H2B-Cerulean
h
Myc Wt : Average Clone Size = 3.60 (n=171 clones)
Myc KO : Average Clone Size = 1.80 (n=113 clones)
% of clones
Clone Size
i
Myc Wt : 260% more cells
Myc KO : 80% more cells
Pancreatic Cells Clonal Expansion P1 to P20
Normalized Nr. of new cells
Clone Size
j
-3.7x
0.0127
Log2 Ratio (Tom+/YFP+)
Control iFlp-Mosaic
Myc LOF iFlp-Mosaic
k
Adult Liver - 2 weeks after genetic induction.
iCre MYFP-MTomato/MTFP1
iFlp H2B-Cherry/GFP/Cerulean
Tg-CAG-FlpOERT2
iFlp MTomato-Cre / MYFP
Control
Myc floxed
MbTomato MbYFP MbTfp1
H2B-Cherry H2B-GFP H2B-Cerulean
50 microns
2n (1 Mononucleated cell)
2x2n (1 Binucleated cell)
2n+2n (2 Mononuclated cells)
mYFP
mTom
mTom+mYFP
mTom+mTFP1
mTom+mYFP+mTFP1
H2B-GFP
H2B-Cherry
H2B-Cer
H2B-GFP+H2B-Cherry
H2B-GFP+H2B-Cer
H2B-Cer+H2B-Cherry
H2B-GFP+H2B-Cer+H2B-Cherry
2n nuclei
4n nuclei
l
MbYFP+
MbTom+
% of clones
Avg. Clone Size = 1.10 (n=261 clones)
m
Myc Wt MbYFP+ (66 dual or tri-labelled clones)
Myc Wt MbTom+ (195 dual or tri-labelled clones)
Control
% of clones
Non-proliferative (2n)
Proliferative (2n)
Non-proliferative (4n)
Proliferative (4n)
n
Control
% clones
mbYFP+
mbTom+
Prolif.
Non-Prolif.
o
-4.2x
Log2 (Ratio Tom+/YFP+)
Control iFlp-Mosaic
Myc LOF iFlp-Mosaic
p
Myc Wt MbYFP+ (67 dual or tri-labelled clones)
Myc KO MbTom+ (62 dual or tri-labelled clones)
Myc floxed
% of clones
Non-proliferative (2n)
Proliferative (2n)
Non-proliferative (4n)
Proliferative (4n)
q
Myc floxed
% clones
mbYFP+
mbTom+
Prolif.
Non-Prolif.

Figure 6

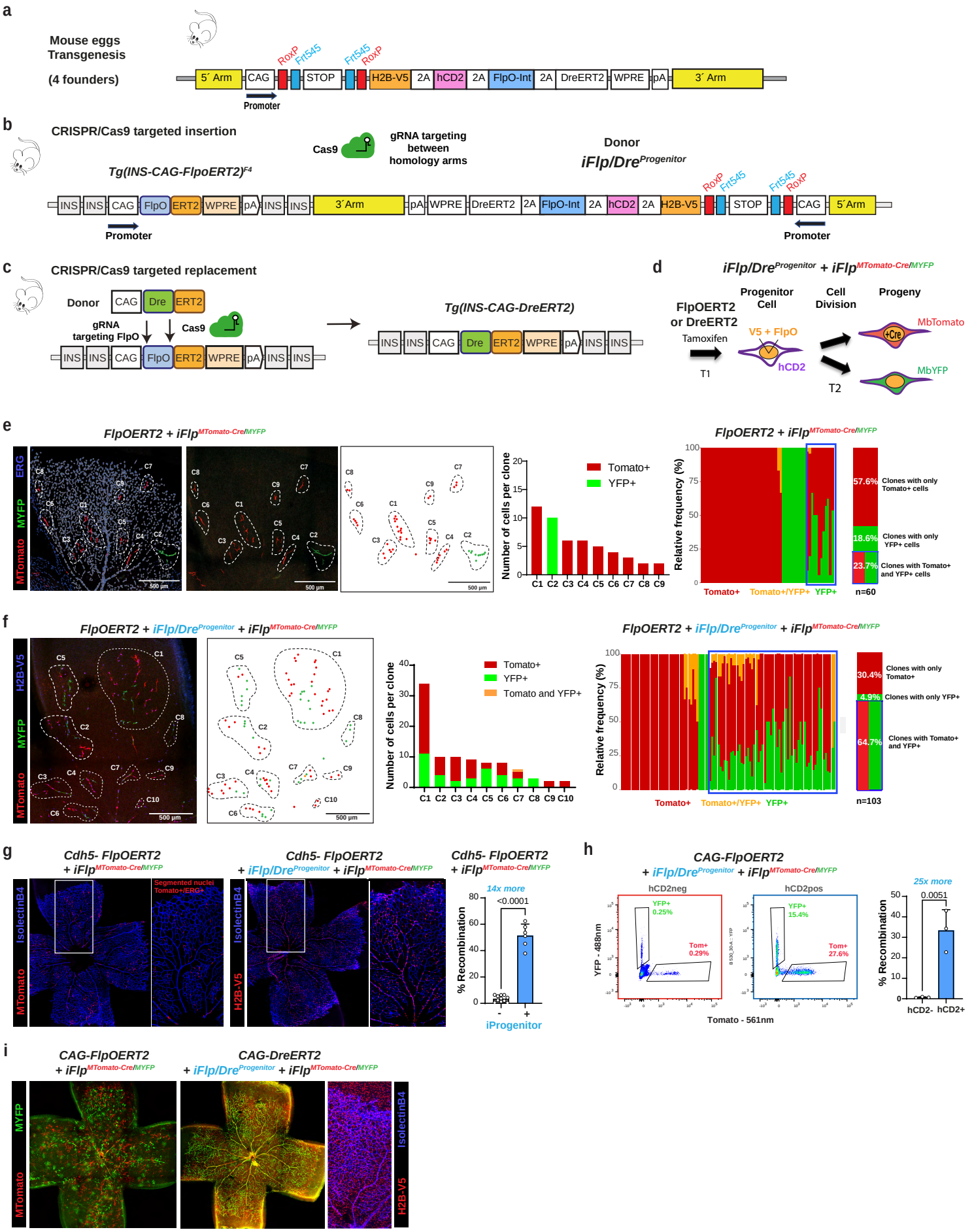
a
Mouse eggs
Transgenesis
(4 founders)
5´ Arm
CAG
Promoter
RoxP
Frt545
STOP
Frt545
RoxP
H2B-V5
2A
hCD2
2A
FlpO-Int
2A
DreERT2
WPRE
pA
3´ Arm
b
CRISPR/Cas9 targeted insertion
Cas9
gRNA targeting between homology arms
Donor
iFlp/Dre Progenitor
Tg(INS-CAG-FlpoERT2)F4
INS
CAG
FlpO
ERT2
WPRE
pA
3´Arm
5´Arm
Promoter
c
CRISPR/Cas9 targeted replacement
Donor
Dre
gRNA targeting FlpO
Tg(INS-CAG-DreERT2)
d
iFlp/Dre Progenitor + iFlp MTomato-Cre/MYFP
FlpOERT2 or DreERT2
Tamoxifen
T1
Progenitor Cell
V5 + FlpO
hCD2
Cell Division
T2
Progeny
MbTomato
+Cre
MbYFP
e
FlpOERT2 + iFlp MTomato-Cre/MYFP
ERG
MYFP
MTomato
500 µm
Number of cells per clone
Tomato+
YFP+
Relative frequency (%)
Tomato+
Tomato+/YFP+
YFP+
57.6% Clones with only Tomato+ cells
18.6% Clones with only YFP+ cells
23.7% Clones with Tomato+ and YFP+ cells
n=60
f
FlpOERT2 + iFlp/Dre Progenitor + iFlp MTomato-Cre/MYFP
H2B-V5
Tomato and YFP+
30.4% Clones with only Tomato+
4.9% Clones with only YFP+
64.7% Clones with Tomato+ and YFP+
n=103
g
Cdh5- FlpOERT2 + iFlp MTomato-Cre/MYFP
Segmented nuclei Tomato+/ERG+
IsolectinB4
MTomato
Cdh5- FlpOERT2 + iFlp/Dre Progenitor + iFlp MTomato-Cre/MYFP
H2B-V5
14x more
<0.0001
% Recombination
iProgenitor
h
CAG-FlpOERT2 + iFlp/Dre Progenitor + iFlp MTomato-Cre/MYFP
hCD2neg
hCD2pos
YFP+ 0.25%
Tom+ 0.29%
YFP+ 15.4%
Tom+ 27.6%
YFP - 488nm
Tomato - 561nm
25x more
0.0051
hCD2-
hCD2+
i
CAG-FlpOERT2 + iFlp MTomato-Cre/MYFP
CAG-DreERT2 + iFlp/Dre Progenitor + iFlp MTomato-Cre/MYFP
MYFP
MTomato
IsolectinB4
H2B-V5

Figure 7

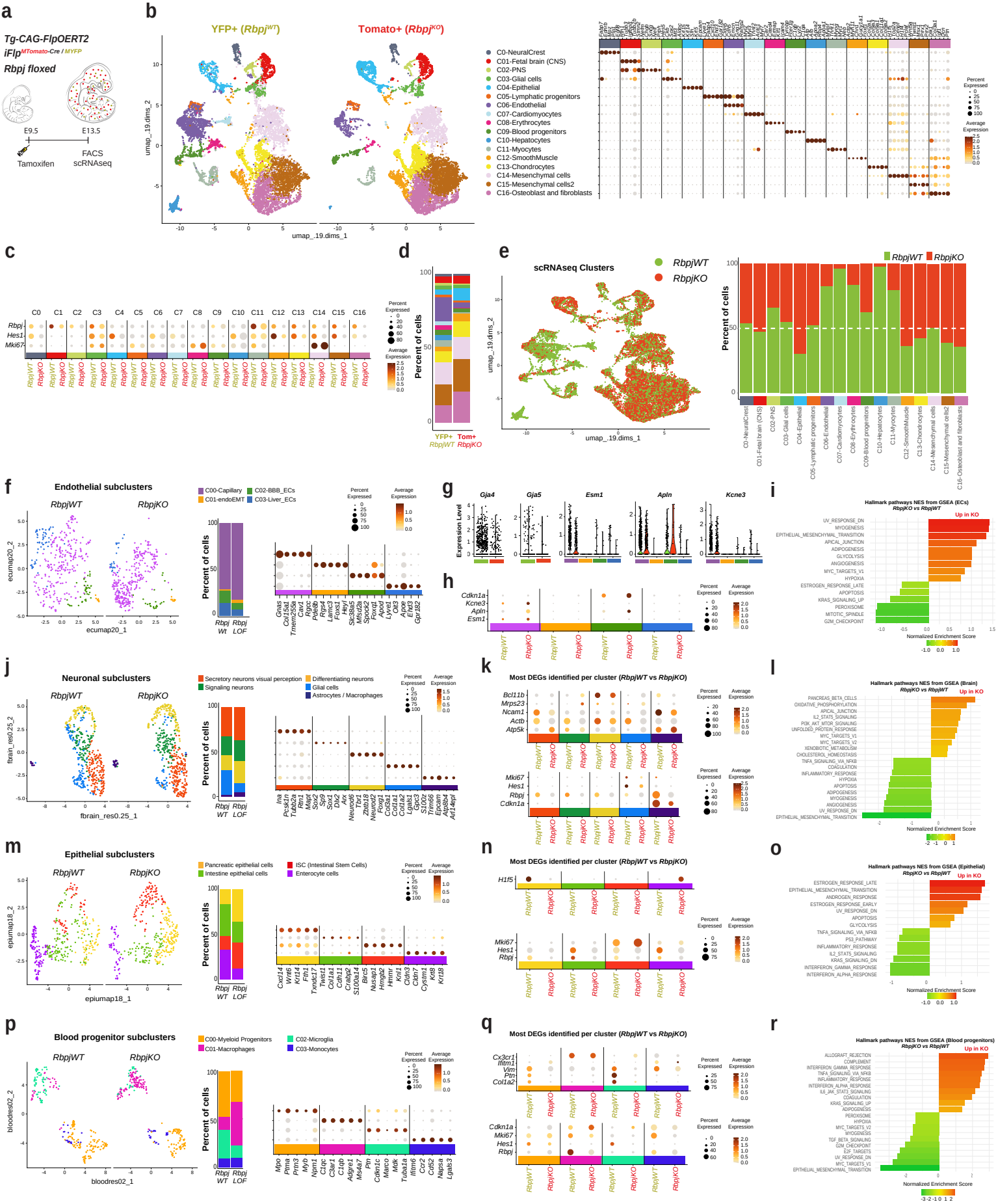
a
Tg-CAG-FlpOERT2
iFlp MTomato-Cre / MYFP
Rbpj floxed
E9.5
E13.5
Tamoxifen
FACS
scRNAseq
b
YFP+ (RbpjWT)
Tomato+ (RbpjKO)
umap_.19.dims_2
umap_.19.dims_1
C0-NeuralCrest
C01-Fetal brain (CNS)
C02-PNS
C03-Glial cells
C04-Epithelial
C05-Lymphatic progenitors
C06-Endothelial
C07-Cardiomyocytes
C08-Erythrocytes
C09-Blood progenitors
C10-Hepatocytes
C11-Myocytes
C12-SmoothMuscle
C13-Chondrocytes
C14-Mesenchymal cells
C15-Mesenchymal cells2
C16-Osteoblast and fibroblasts
Percent Expressed
Average Expression
c
Rbpj
Hes1
Mki67
d
Percent of cells
YFP+ RbpjWT
Tom+ RbpjKO
e
scRNAseq Clusters
RbpjWT
RbpjKO
umap_.19.dims_2
umap_.19.dims_1
Percent of cells
f
Endothelial subclusters
RbpjWT
RbpjKO
C00-Capillary
C01-endoEMT
C02-BBB_ECs
C03-Liver_ECs
ecumap20_2
ecumap20_1
Percent of cells
Rbpj Wt
Rbpj LOF
g
Gja4
Gja5
Esm1
Apln
Kcne3
Expression Level
h
Cdkn1a
Kcne3
Apln
Esm1
i
Hallmark pathways NES from GSEA (ECs)
RbpjKO vs RbpjWT
Up in KO
Normalized Enrichment Score
j
Neuronal subclusters
RbpjWT
RbpjKO
Secretory neurons visual perception
Signaling neurons
Differentiating neurons
Glial cells
Astrocytes / Macrophages
fbrain_res0.25_2
fbrain_res0.25_1
Percent of cells
Rbpj WT
Rbpj LOF
k
Most DEGs identified per cluster (RbpjWT vs RbpjKO)
Bcl11b
Mrps23
Ncam1
Actb
Atp5k
Mki67
Hes1
Rbpj
Cdkn1a
l
Hallmark pathways NES from GSEA (Brain)
RbpjKO vs RbpjWT
Up in KO
Normalized Enrichment Score
m
Epithelial subclusters
RbpjWT
RbpjKO
Pancreatic epithelial cells
Intestine epithelial cells
ISC (Intestinal Stem Cells)
Enterocyte cells
epiumap18_2
epiumap18_1
Percent of cells
Rbpj WT
Rbpj LOF
n
Most DEGs identified per cluster (RbpjWT vs RbpjKO)
H1f5
Mki67
Hes1
Rbpj
o
Hallmark pathways NES from GSEA (Epithelial)
RbpjKO vs RbpjWT
Up in KO
Normalized Enrichment Score
p
Blood progenitor subclusters
RbpjWT
RbpjKO
C00-Myeloid Progenitors
C01-Macrophages
C02-Microglia
C03-Monocytes
bloodres02_2
bloodres02_1
Percent of cells
Rbpj WT
Rbpj LOF
q
Most DEGs identified per cluster (RbpjWT vs RbpjKO)
Cx3cr1
Ifitm1
Vim
Ptn
Col1a2
Cdkn1a
Mki67
Hes1
Rbpj
r
Hallmark pathways NES from GSEA (Blood progenitors)
RbpjKO vs RbpjWT
Up in KO
Normalized Enrichment Score

Supplementary Fig. 1

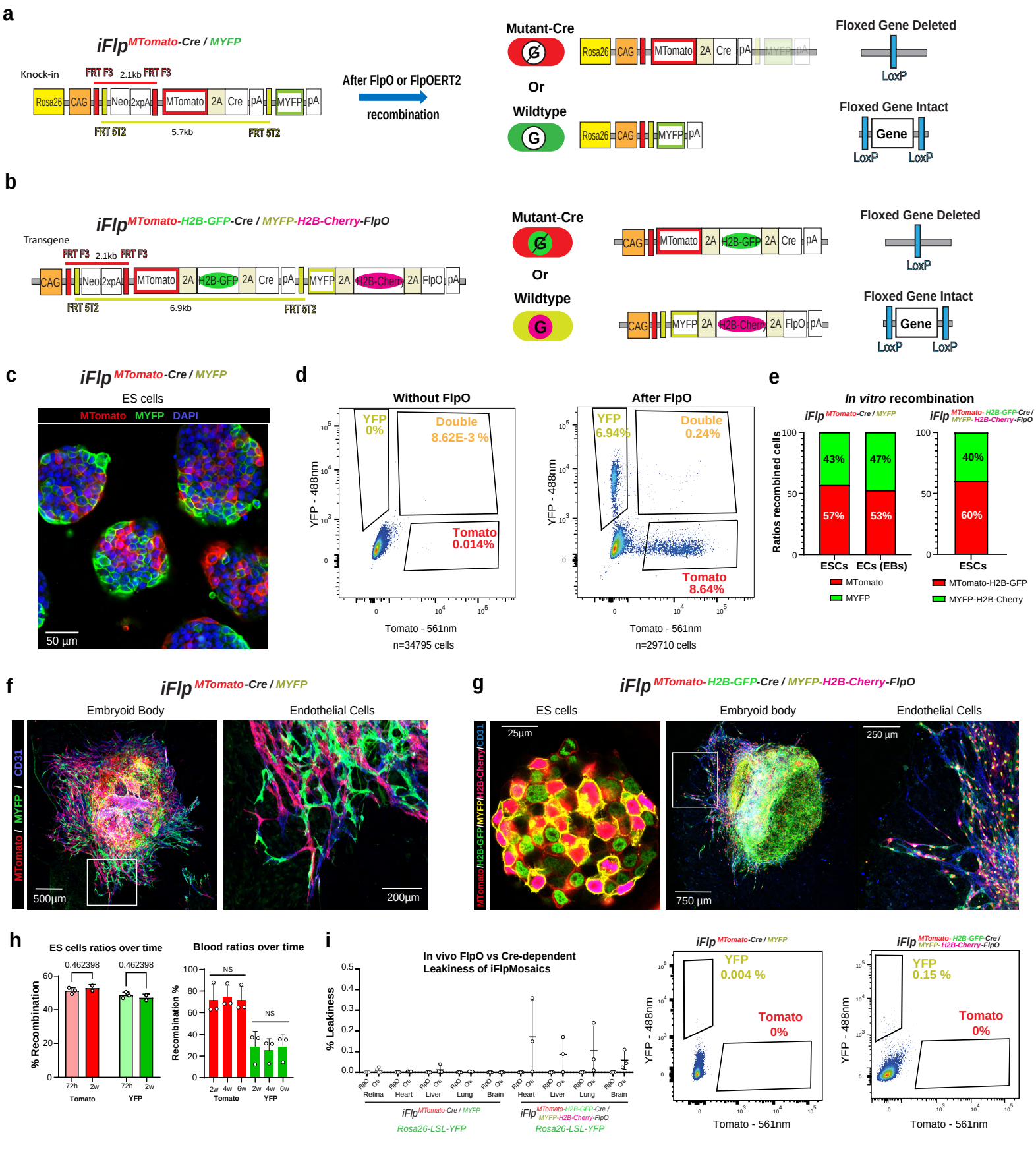

Supplementary Fig. 2

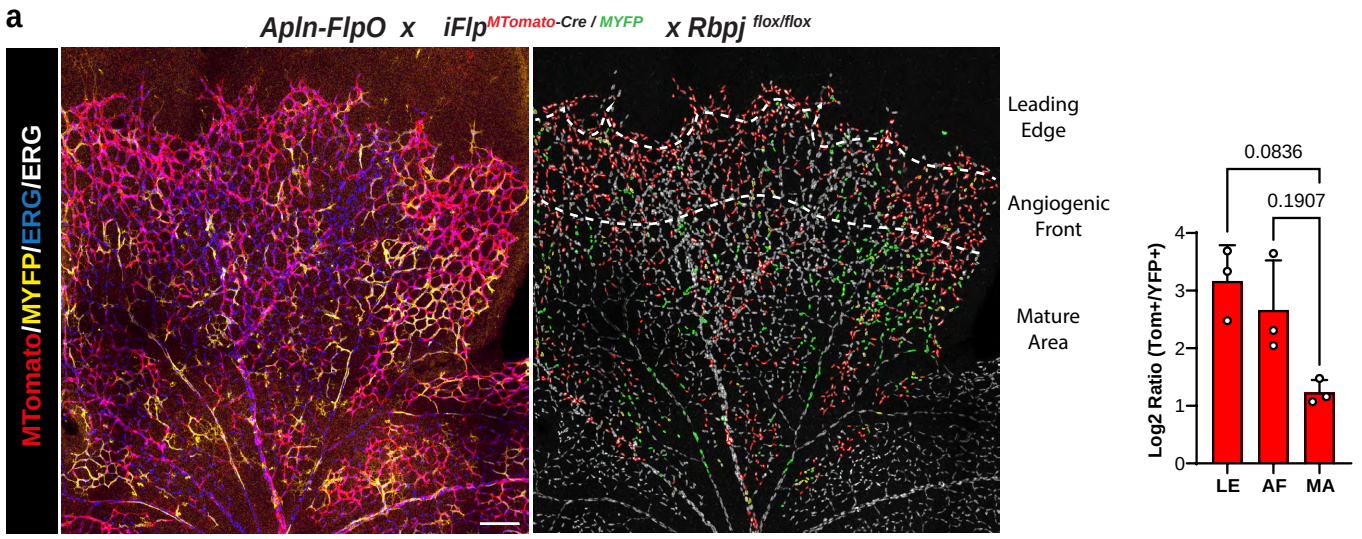

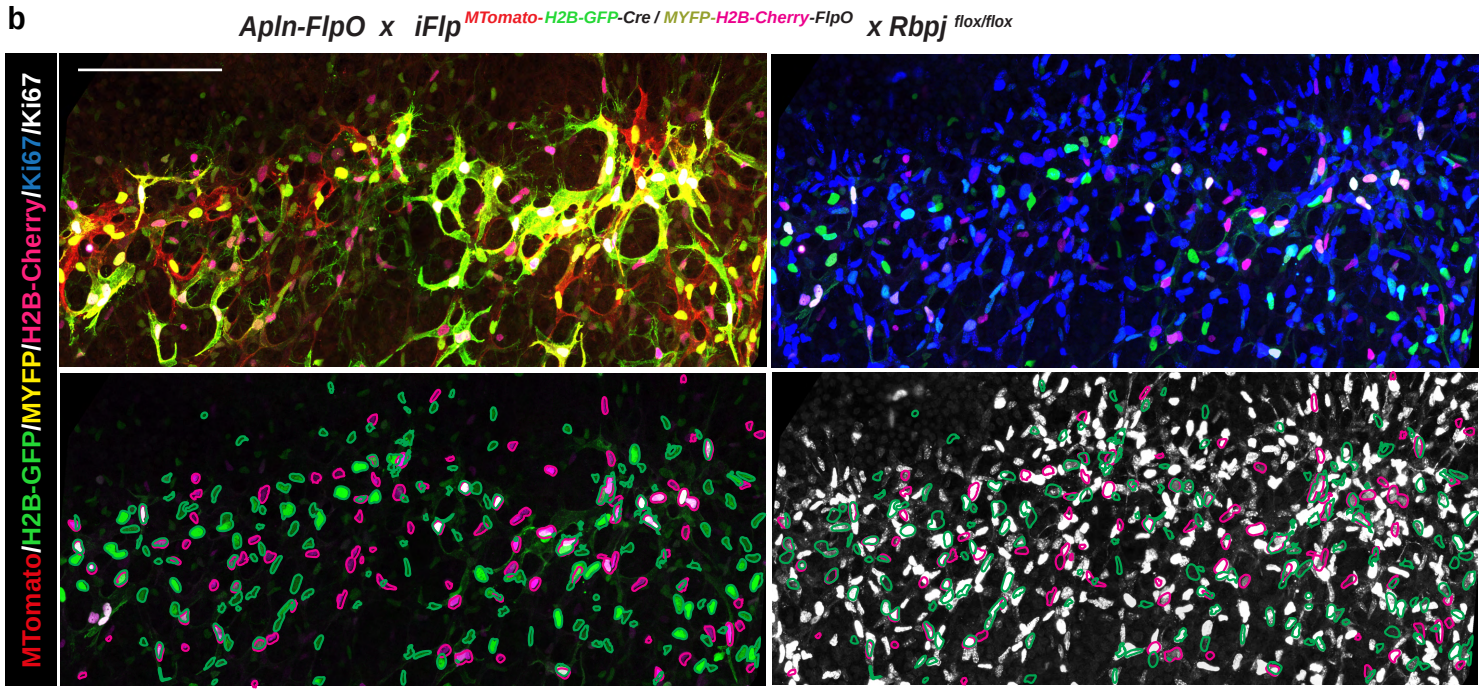

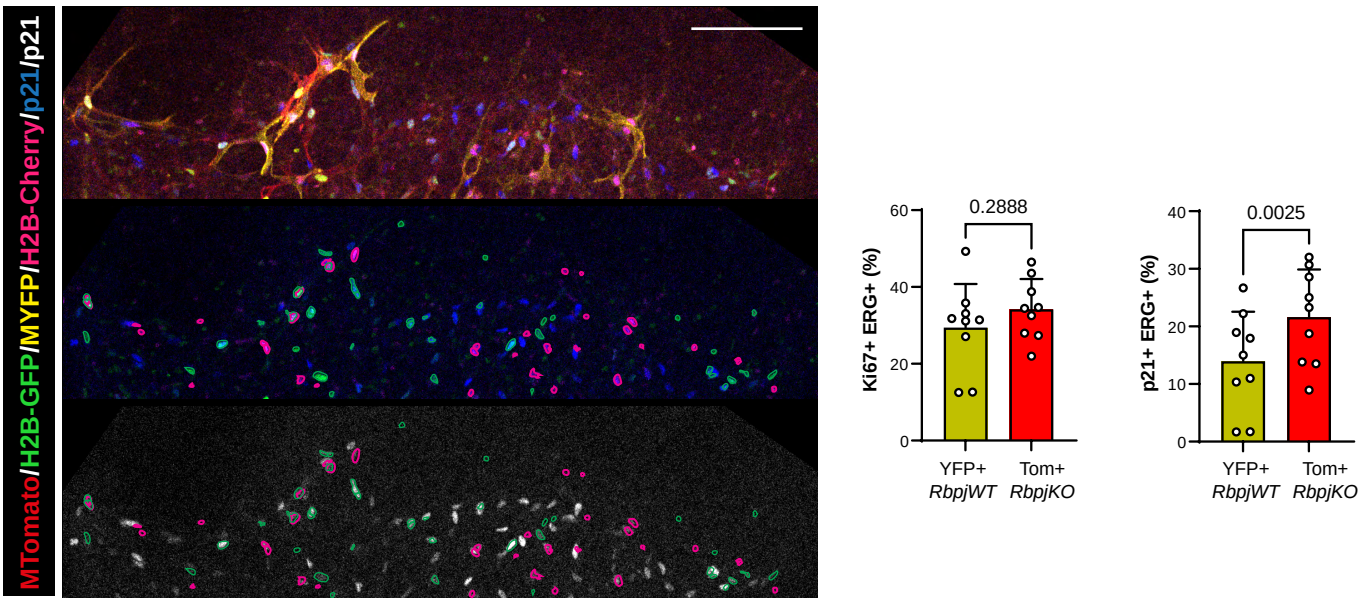

Supplementary Fig. 3

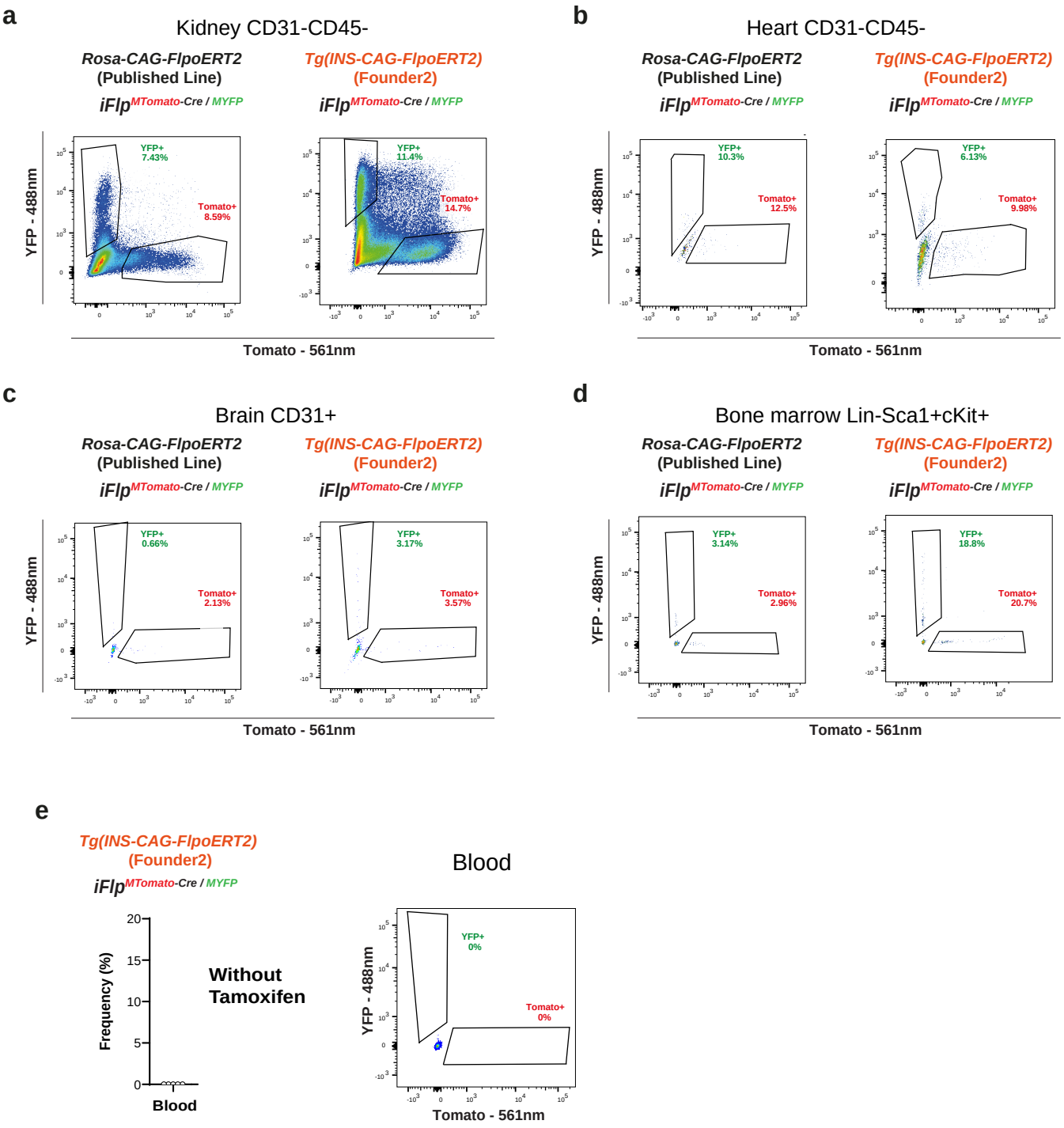

Supplementary Fig. 4

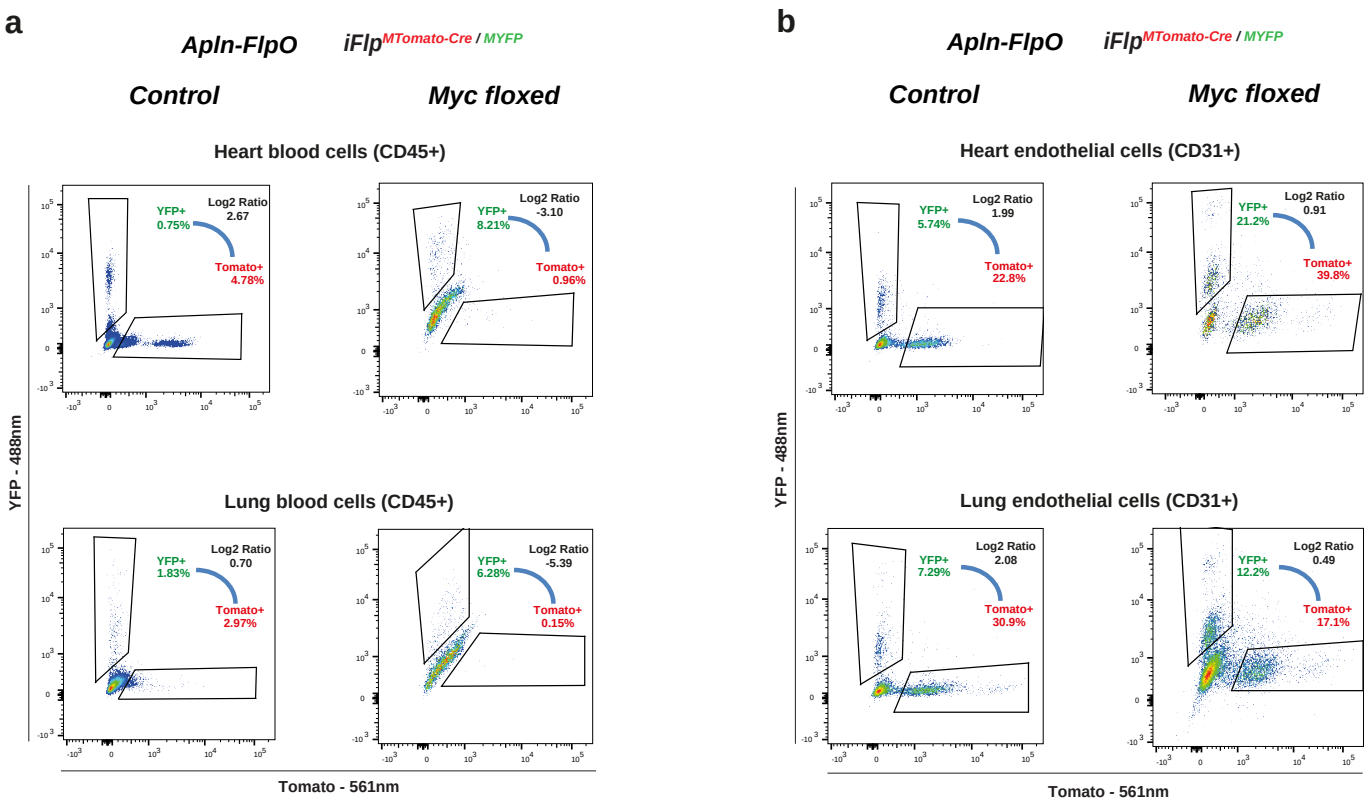

Supplementary Fig. 5

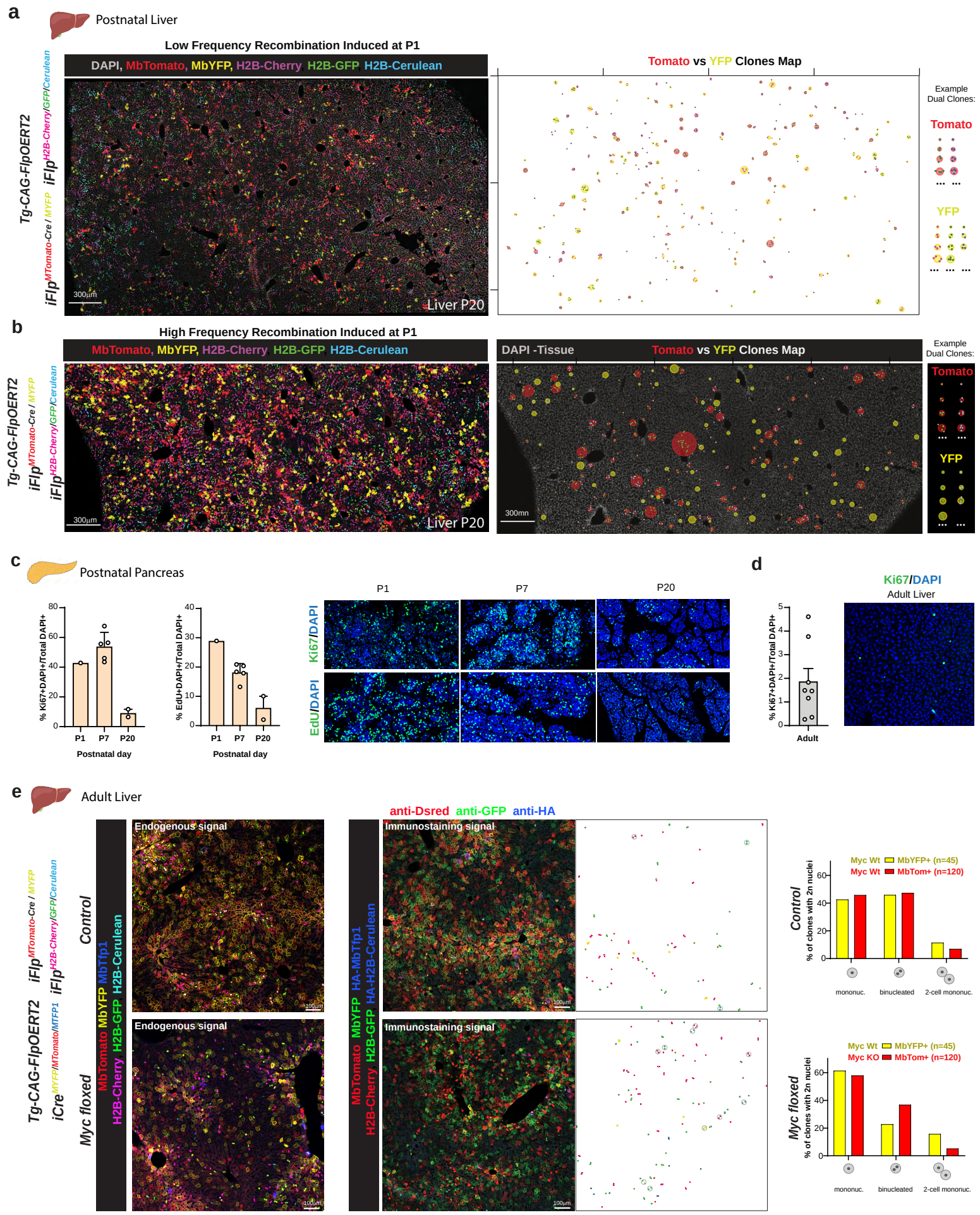

Supplementary Figure 6

a

FlpOERT2 + iFlp/Dre^{Progenitor} + iFlp$^{MTomato\text{-}Cre/MYFP}$

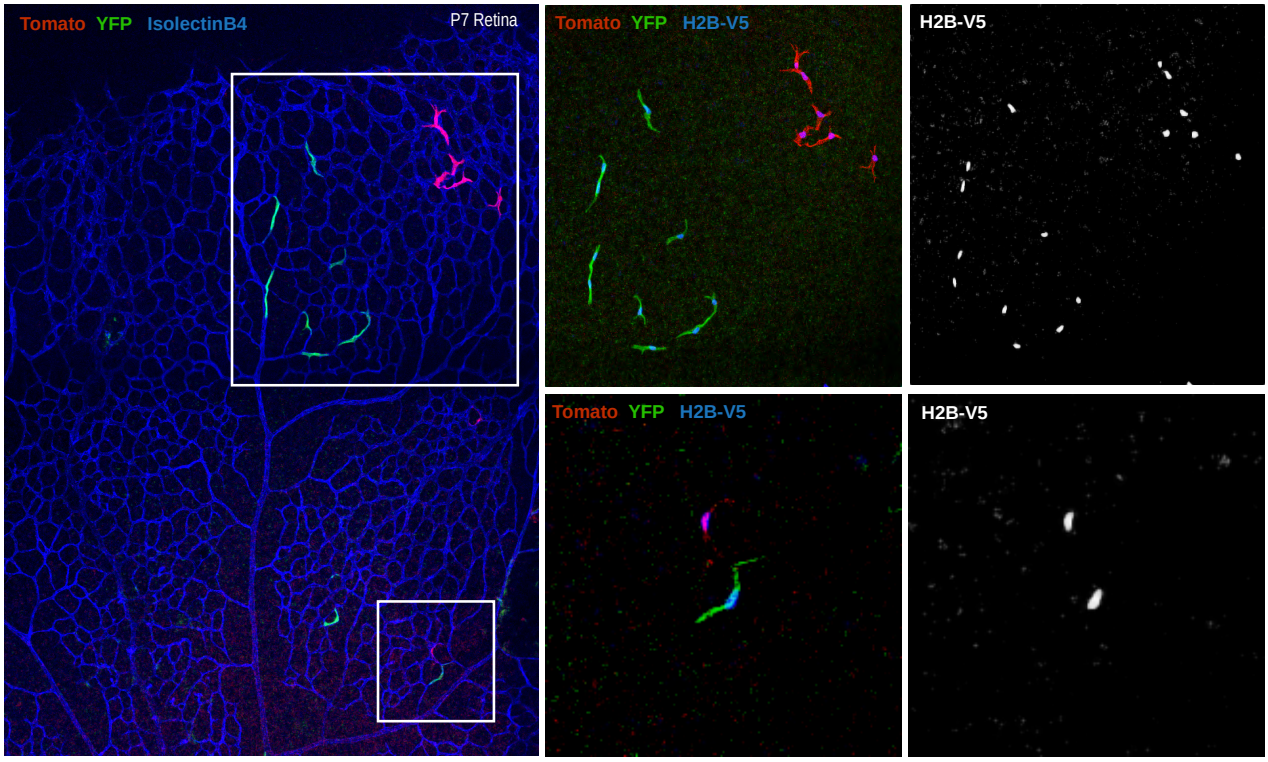
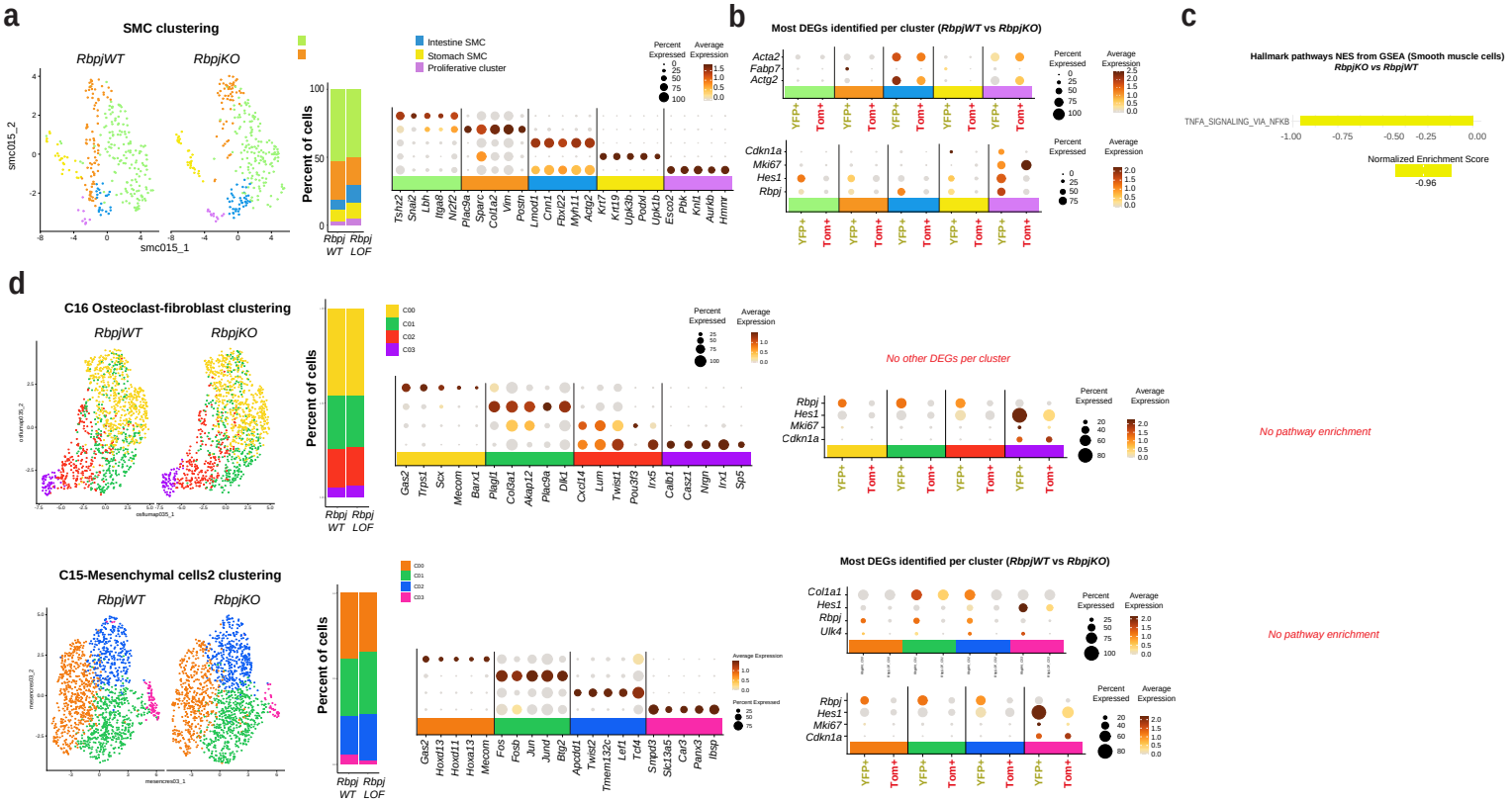
Supplementary Figure 7